International Journal of Plasticity 125 (2020) 1–26

Contents lists available at ScienceDirect

International Journal of Plasticity

journal homepage: www.elsevier.com/locate/ijplas

Microstructure and texture evolution in Mg/Nb layered materials made by accumulative roll bonding

Daniel J. Savage[a], Irene J. Beyerlein[b], Nathan A. Mara[c], Sven C. Vogel[d], Rodney J. McCabe[e], Marko Knezevic[a,*]

[a] Department of Mechanical Engineering, University of New Hampshire, Durham, NH, 03824, USA
[b] Mechanical Engineering Department, Materials Department, University of California at Santa Barbara, Santa Barbara, CA, 93106, USA
[c] Department of Chemical Engineering and Materials Science, University of Minnesota, Minneapolis, MN, 55455, USA
[d] Los Alamos Neutron Science Center, Los Alamos National Laboratory, Los Alamos, NM, 87544, USA
[e] Materials Science and Technology Division, Los Alamos National Laboratory, Los Alamos, NM, 87544, USA

ARTICLE INFO

Keywords:
Crystallographic texture
Twinning
Crystal plasticity
Rolling
Magnesium alloys

ABSTRACT

In this work, lamellar composite sheets combining one of two fully hexagonal magnesium-lithium alloys (Mg–4Li and Mg–5Li wt%) and pure niobium (Nb) are manufactured via accumulative roll bonding (ARB). With extreme straining of over two true strain, the individual layers were refined to 200 μm. The strength differential between co-deforming phases with strain is characterized to be low enough to facilitate bonding without instabilities. Additionally, homogeneity in deformation was enhanced by intermediate annealing, especially for the Mg-xLi phase. Diffraction methods and polycrystal modeling are employed to study the microstructure and texture evolution of the individual phases after each subsequent ARB pass. Characterization by electron backscatter diffraction and neutron diffraction reveals substantial changes in microstructure and texture in both phases and very little deformation twinning in the Mg-xLi phase. Evolution of grain morphology and the number of grains that span a layer with ARB and annealing are determined and discussed. To link texture evolution to slip-based deformation mechanisms during the processing, a multiscale polycrystalline model of the two-phase Mg–4Li/Nb composite was developed, which included a relative directional compliance (RDC) method to account for anisotropic interactions in the phases, allowing appropriate slip sensitivity to dislocation density based hardening on the multiple slip modes in Mg–4Li and in Nb. The model indicates that the deformation of the Mg–4Li phase during ARB cycles was accommodated by more basal $< \mathbf{a} >$ and progressively smaller amounts of prismatic $< \mathbf{a} >$, pyramidal $< \mathbf{c}+\mathbf{a} >$, and twinning than previously reported for rolling of Mg–4Li. The experimental textures cannot be entirely explained by grain shape and an increase in pyramidal and prismatic slip resistance are required as expected with a small grain size. Consistent with measurements, the model predicts that **c**-axis of the Mg–4Li phase tilts from the sheet's normal direction towards the rolling direction, and that the strong γ-fiber and the unusually weak α-fiber should develop in Nb with large ARB straining of the Mg-xLi/Nb composites.

* Corresponding author. University of New Hampshire, Department of Mechanical Engineering, 33 Academic Way, Kingsbury Hall, W119, Durham, NH, 03824, United States.
E-mail address: marko.knezevic@unh.edu (M. Knezevic).

https://doi.org/10.1016/j.ijplas.2019.08.015
Received 22 December 2018; Received in revised form 31 July 2019; Accepted 21 August 2019
Available online 26 August 2019

1. Introduction

Severe plastic deformation (SPD) techniques are metal forming processes that can successfully refine the microstructure of single-phase and multi-phase materials while retaining the sample's pre-deformed dimensions (Dinda et al., 2005; Jahedi et al., 2015a, 2015b, 2017b; Saito et al., 1999; Valiev et al., 2000). For some material systems, fine-grained to nano-crystalline materials can be produced via accumulative roll bonding (ARB), the metal forming method developed in 1999 (Saito et al., 1999). Examples include Cu/Nb (Carpenter et al., 2014), Cu/Ta (Zeng et al., 2016), Cu/Ni (Tayyebi and Eghbali, 2013), and Ag/Fe (Yasuda and Kikuchi, 2004). In these cases, five-to ten-fold enhancements in the strength of the constituent phases were achieved. The initial metals were pure and soft, and during processing major instabilities, such as cracking or shear banding, did not hinder the layer refinement. In these cases, the metals were either face-centered cubic (FCC) or body-centered cubic (BCC).

Metal-metal composites have been used in industry for decades (Bay, 1986; Cave, 1973; Jahedi et al., 2017a; Milner and VAIDYANATH, 1960; Yahiro et al., 1991; Zare et al., 2016a, b). In particular, roll bonding - and more recently ARB - offers attractive routes to produce advanced metal-metal composites because they are scalable and are the most advantageous processes for continuous production of plates and sheets (Li et al., 2008). The ARB process extends the processing space of roll bonding by allowing the tuning of the microstructure to interface driven properties such as thermal stability, phase stability, and deformation mechanisms (Mara and Beyerlein, 2015; Misra and Hoagland, 2007; Pathak et al., 2017; Zeng et al., 2016) which can facilitate new applications of materials in industry. In rolling metal-metal composites, a high interfacial pressure facilitates bonding by adhesion, which requires a clean bonding surface and that the interfaces of the metal-metal composites are interatomic distances apart (Cave, 1973; Milner and VAIDYANATH, 1960). In practice, cleanliness and atmosphere can make bonding difficult due to contamination and reactions such as oxide formation. Thus cold welding with scratch-brushed surfaces or other surface-roughening methods are common since this facilitates two potential mechanisms for a clean bonding surface formation (Bay, 1983): i) the scratch brushing forms a brittle material layer that fractures, and material is extruded through cracks, and ii) fracturing of a contamination film or oxide which facilitates extrusion of material through cracks. With each ARB pass, prior interfaces are expected to improve as the contaminate is stretched along the interface. The cold pressure bonding method lends itself to a wide range of materials. For instance, the Mg-xLi/Nb composite phases studied in this paper are not expected to join directly to each other with other traditional joining methods such as friction stir welding, interface diffusion, and other conventional welding techniques due to immiscibility and thermal properties of the phases (Song et al., 2018).

Magnesium (Mg) is one metal in particular that could benefit from microstructural refinement. Mg in pure and most alloyed forms is weak; with nano-structuring, Mg could be made stronger and potentially more ductile depending, for instance, on how grain size affects slip resistances or how grain size affects temperature dependence for superplasticity (Figueiredo et al., 2014). The potential for interface constrained refinement can be seen by recent work on Mg/Nb thin films, in which the composite consisting of alternating pure Mg and pure Nb layers achieved high strength and moderate ductility (Ardeljan et al., 2018; Ham and Zhang, 2011; Pathak et al., 2017). While it is possible to make a bulk layered material via ARB, Mg has a hexagonal close-packed (HCP) crystal structure, which is more challenging to plastically deform due to pronounced anisotropy. In prior works, several HCP/BCC combinations have been attempted using ARB with some success, e.g. Al/Zn (Dehsorkhi et al., 2011), Mg/Al (Chang et al., 2012), Ti/Al (Yang et al., 2010), Cu/Zn (Ghalandari et al., 2014) and Al/Mg/Ti (Motevalli and Eghbali, 2015) as micro-laminate systems, and Cu/Zr (Sun et al., 2010) and Zr/Nb (Carpenter et al., 2015a, 2015b; Knezevic and Beyerlein, 2018) as nano-laminate systems. Some of these have included Mg as one phase. With HCP systems, shear bands often form early in the process while the layers are still several hundreds of microns in thickness (Ardeljan et al., 2015). Recent works in nano-structuring of Zr/Nb via ARB prevented the formation of shear bands by intermediate annealing (Carpenter et al., 2015a). Subsequent modeling work suggested that annealing had the effect of lowering the dislocation density, and with it the plastic anisotropy in the Zr crystals (Ardeljan et al., 2015).

In this work, we apply the methodology used for Zr/Nb to ARB fully HCP Mg–4Li and Mg–5Li (wt%) alloys with Nb. The HCP Mg-xLi alloys were chosen due to their relatively more ductile behavior at room temperature when compared to other Mg alloys. They exhibit sufficient strength to be roll bonded with Nb, and they remain immiscible with Nb (de Boer et al., 1980; Niessen et al., 1983), limiting the potential for interface mixing (Agnew et al., 2006; Lentz et al., 2016; Risse et al., 2017). The prior polycrystal modeling suggested that deformation of this material in uniaxial loading and rolling took place mainly by basal and prismatic slip and moderate levels of type one and type two pyramidal $< \mathbf{c}+\mathbf{a} >$ slip (Zecevic et al., 2018a). In addition, previous modeling studies in combination with analysis of twinning via twin/matrix misorientation analysis of electron backscatter diffraction (EBSD) maps indicated that tensile $\{10\bar{1}2\} < \bar{1}011 >$ deformation twinning contributes little to the deformation of this alloy, especially for fine grain initial microstructures (Lentz et al., 2016). Here, with intermediate annealing between ARB passes, we were able to fabricate Mg-xLi/Nb layered composites with an average of ~200 μm layers. EBSD characterization of the microstructure after every pass finds that deformation twinning occurred at similar frequencies to the twin fractions reported in (Lentz et al., 2016) for simple compression. Indeed, after an ARB pass and anneal cycle, a fine grain initial microstructure further suppresses twinning, promoting more homogeneous deformation. The EBSD analysis also suggests some dynamic recrystallization occurs in the Mg-xLi during the ARB process. To associate the deformation textures with deformation mechanisms, we employ an elasto-plastic self-consistent (EPSC) polycrystal model with a relative directional compliance (RDC) scheme to treat the interactions in the Mg and Nb layers independently (Takajo et al., 2019; Tomé, 1999). Texture evolution measured by neutron diffraction combined with polycrystal modeling indicates that the deformation of the Mg phase was dominated by basal and prismatic $< \mathbf{a} >$ slip at low strain and by a combination of $< \mathbf{a} >$ and some amount of $< \mathbf{c}+\mathbf{a} >$ at higher strain.

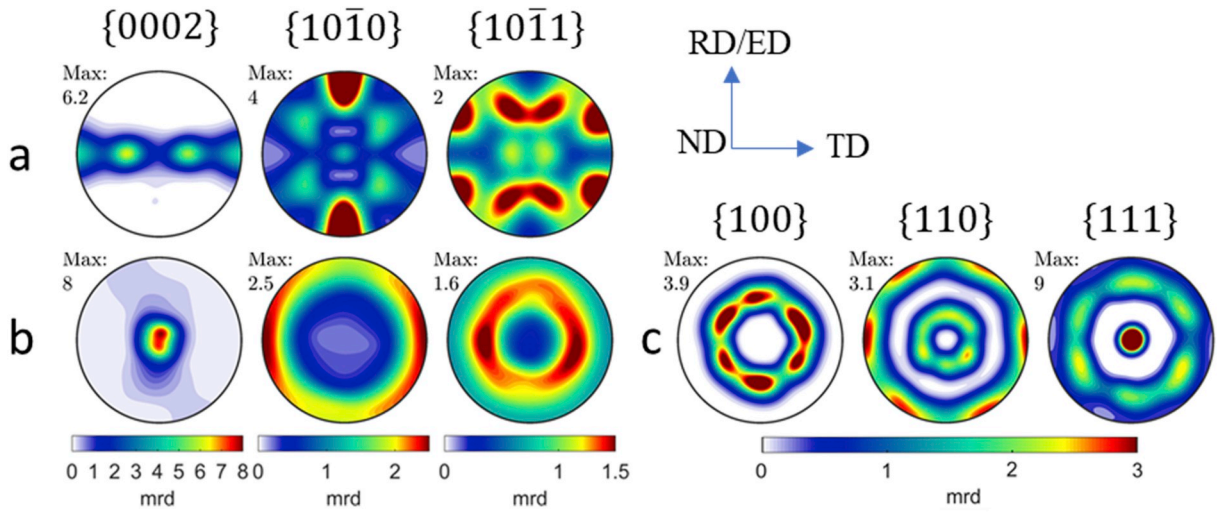

Fig. 1. Initial textures of (a) hot extruded Mg–4Li, (b) rolled Mg–5Li, and (c) annealed Nb.

2. Experimental methods

2.1. Materials

Two types of HCP Mg-xLi alloys are utilized, Mg–4Li and Mg–5Li (wt. %), which are considered as some of the lightest structural alloys. Sheets of the Mg-xLi were obtained from the Leibniz Universität Hannover (Institut für Werkstoffkunde) which hot extruded the alloys with a ratio of 41:1 and a billet temperature of 300°C followed by air cooling. The Mg–5Li was further processed by rolling. The Mg–4Li material has been extensively characterized in previous works (Lentz et al., 2015, 2016; Risse et al., 2017; Zecevic et al., 2018a) whose investigation of microstructure are summarized here. Sheets that were air cooled resulted in a uniform average grain size of 38 μm (Risse et al., 2017). Investigation of the material by scanning electron microscopy and energy dispersive spectroscopy dispersed Al–Si rich phases that form necklacing structures along the extrusion direction. The modeling work of (Risse et al., 2017) concluded that these precipitates were in low enough volume fraction so as to have no significant impact on the slip behavior. The Mg–4Li extruded sheet texture Fig. 1a consists of basal poles dispersed between TD and ND and a strong prismatic pole aligned with RD. The Mg–5Li extruded sheet exhibits a rolling texture in Fig. 1b with basal poles slightly split in RD and prismatic poles aligned with TD. While pre-straining and annealing substantially change the Mg–4Li texture and microstructure for the ARB process, the Mg–5Li rolling texture and microstructure do not evolve substantially throughout the ARB process.

The composition for the Nb obtained from ATI-Wah Chang in wt. ppm is C < 20, Fe < 25, H < 3, Hf < 30, Mo < 30, N < 20, Ni < 20, O < 40, P < 30, Si < 25, Ta = 110, Ti < 30, W < 30, Zr < 30, and Nb balance. The Nb sheet was rolled and heat treated as in Cu/Nb and Zr/Nb to fully anneal the microstructure and grow large grains. As reported in previous works (Knezevic et al., 2014c), equiaxed grains of approximately 300 μm in size are achieved, larger than that of Mg-xLi by over an order of magnitude. The Nb exhibited a <111> fiber texture parallel with the normal direction (ND) of the plate as shown in Fig. 1c.

2.2. Accumulative roll bonding (ARB) of Mg–Li alloys with Nb

The ARB process was applied to form micro-laminates of Mg–4Li/Nb and Mg–5Li/Nb. Prior to roll bonding, the Mg–4Li, Mg–5Li, and Nb materials were pre-strained and annealed. A ~30% rolling reduction improved the surface quality and achieved the target

Table 1
List of Mg–4Li/Nb and Mg–5Li/Nb layered sample statistics measured from the geometry of the ARB processed sheets. Note that the true strain is cumulative for the ARB composite, wherein pre-straining and the strain resetting of Mg–4Li/Mg–5Li by annealing are disregarded. Note also that the top and the bottom layer of the Mg–4Li/Mg–5Li phase are considered as one.

Mg–4Li						Mg–5Li					
Number of layers	h_{Mg}, [μm]	h_{Nb}, [μm]	ε	Process step	Anneal temp. (°C)	Number of layers	h_{Mg}, [μm]	h_{Nb}, [μm]	ε	Process step	Anneal temp. (°C)
1	2489	2032	0	–	–	1	2082	2032	0	–	–
2	1190	971	0.74	ARB 1	200	2	1163	1118	0.58	ARB 1	200
4	520	425	1.56	ARB 2	200	6	520	500	1.39	ARB 2	200
12	214	174	2.45	ARB 3	200	12	212	204	2.28	ARB 3	200

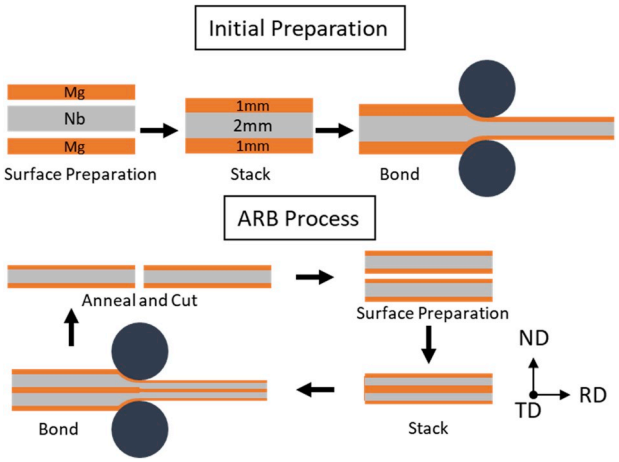

Fig. 2. A schematic description of the ARB process utilized to make Mg-xLi/Nb metal laminates.

thickness needed for rolling with the Nb in a metal/metal laminate consisting of similar volume fractions. Due to the initial stacking sequence of the Mg alloy and Nb, the layer thickness, h_{Mg} and h_{Nb}, reported in Table 1 are representative of the nominal layer thickness for Mg-xLi and Nb layers respectively measured with a micrometer, and we assume the cladding layers to be approximately $h_{Mg}/2$. The total strain due to ARB is reported using the h_{Mg}, i.e. the total strain is $\varepsilon = \ln\left(\frac{h_{Mg,0}}{h_{Mg}}\right)$where $h_{Mg,0}$ is the layer thickness of the Mg alloy before the first ARB pass. Before being processed by ARB, the Nb was annealed at 950 °C, and Mg-xLi was annealed at 200 °C in a vacuum furnace and allowed to cool in the furnace under vacuum. The purpose of the anneals are threefold: 1) to improve homogenous deformation by creating a uniform microstructure of equiaxed grains, 2) to lower dislocation content, thereby maximizing the amount of work hardening, and 3) to maximize boundary strengthening in Mg-xLi and minimize boundary strengthening in Nb.

The ARB process applied here, schematically shown in Fig. 2, follows that which was used in a previous HCP/BCC system consisting of pure Zr and Nb (Carpenter et al., 2015a; Carpenter et al., 2015b), with the exception of the heat treatment temperature that is applied to both the Mg–4Li/Nb and Mg–5Li/Nb composites. The initial ARB stack consisted of the Mg alloy cladding and the Nb core. The initial stack dimensions were 3.5″ x 6″ and ~4 mm thick. After cutting to the appropriate dimensions, the stack was cleaned in an ultrasonic cleaner using acetone for 10 min. A steel wire brush on a power drill was then used to remove oxides and provide a suitably roughened surface for bonding. After this, the sample was rolled on a Waterbury Farrel rolling mill (the same as configuration used for Cu/Nb and Zr/Nb work) with a roll diameter of 16″ at room temperature. Similar to prior roll bonding studies, we found that 50–55% reduction provided sufficient bond strength to cut and work with the Mg-xLi/Nb after it had been rolled.

After each rolling step, the composite was annealed at 200 °C for 1 h and allowed to furnace cool, which recrystallizes and stress relieves the Mg-xLi microstructure but does not affect the Nb microstructure. The edge-cracked material and leading and trailing edges were then removed via a shear, the material cut in half, stacked, and rolled again. This process was repeated three times, each denoted in the paper as ARB 1, ARB 2, and ARB 3. The final layer thickness was approximately 200 μm for both the Mg–4Li/Nb and Mg–5Li/Nb composites. Table 1 summarizes the samples made with Mg–4Li material (left side) and Mg–5Li material (right side). The features listed are the number of layers, average thickness after the roll bonding processing step, total strain, sample label as the ARB process step, and post-annealing temperature.

Attempts to repeat the annealing/roll bonding steps for a fourth time on these samples led to shear failure through thickness. Specifically, for the Mg–4Li/Nb composite, the sample was 1″ wide due to edge crack removal and completely failed by shear through thickness during the fourth rolling pass. For the Mg–5Li/Nb composite, the sample required less material removal, due to edge cracking, but split down the middle during the third ARB process, resulting in approximately 1″ strips. During the fourth ARB attempt, the sample failed in a similar manner to the Mg–4Li/Nb. However, continuous rolling (not ARB of the stacked sheets but only thickness reduction by straight rolling of an individual sheet) was possible with no fracture occurring. This suggests geometry and reduction played an important role in the failure of the fourth ARB pass. These continuously rolled samples were not studied hereinafter. The results presented in this paper represent the best of several ARB attempts, and success varied for similar processing parameters. The sensitivity of the result to processing parameters and the failure mode suggests that future attempts should use elevated temperatures during rolling and/or higher rolling speeds to enhance formability.

2.3. Texture characterization

Neutron diffraction was performed on both the initial materials and processed samples using the High Pressure Preferred Orientation (HIPPO) neutron time-of-flight diffractometer at the Los Alamos Neutron Science Center at Los Alamos National Laboratory (LANL) (Barrett et al., 2019; Vogel et al., 2004; Wenk et al., 2003). Unlike x-ray diffraction or EBSD, neutron diffraction provides a bulk measurement of specimen texture. The techniques used for both the collection of neutron diffraction data and the

accompanying analysis to capture phase-specific orientation distribution functions (ODFs) was consistent with those described for the Cu/Nb and Zr/Nb systems (Carpenter et al., 2012). A small change within the HIPPO diffractometer set-up is the addition of two new detector panels at $2\theta = 60^{\circ}$ and 120°. Approximately $1 \times 1 \times 0.2$ cm sized specimens were cut from the center of the ARB plates and used for the neutron diffraction. The composite samples in the as-rolled and annealed state for which the Nb, Mg–4Li, and Mg–5Li phase textures were measured are listed in Table 1. Consistent with x-ray diffraction and scanning electron microscopy performed in (Risse et al., 2017), no Mg–Li beta phase was evident in the neutron scattering data given the lattice parameter reported in literature (Edalati et al., 2017).

2.4. Microstructure characterization

EBSD was performed on the as rolled (AR) and annealed (AN) ARB samples to analyze the phase grain morphology and investigate the possibility of twinning and its twinning type and fraction. While extensive EBSD studies that would cover spatial variation across the laminate would be ideal, this is not a tractable experimental approach. In light of the heavily deformed material and relatively uniform layer refinement, we have chosen to collect at least one EBSD scan per sample containing on the order of a few thousand grains that produces similar textures to that produced by neutron diffraction.

Critical to the success of EBSD evaluation was the sample preparation for the two-phase Mg-xLi/Nb sample. These two metals have different hardness and chemical reactivity, making an EBSD quality surface challenging. All samples were mounted in epoxy resin. For the Mg phase, the surfaces were ground with SiC to 800 grit using water as the lubricant. The samples were then polished from 30 μm to 1 μm using 3 M AlOx polish paper discs, again using water for a lubricant. The final stages of preparation for Mg involved swabbing with 2% Nital followed by a rinse in Ethanol and drying in a stream of warm air. The Nb surfaces were prepared with a hydrofluoric acid-based etch. For Knoop microhardness testing, which was performed to ASTM standard E384 with a 50 gf load, Nb was finished using Allied High Tech Colloidal Silica and the Mg was finished with Buehler Masterprep.

Due to the poor EBSD pattern indexing in the highly strained Mg-xLi phase, the effect of preferential etching and the effect of phase pattern contrast on background reconstruction was addressed in EBSD pattern (EBSP) post-processing. The Mg-xLi EBSPs were collected without a background and with a fine step size of 130 nm. The raw EBSPs were neighbor averaged on a hexagonal grid before a background was reconstructed in TSL OIM8 analysis for the phase of interest. This has the effect of smoothing spurious background contributions due to etch induced topography. The SE image and chemical analysis collected with the EBSPs were used to isolate one phase during the background reconstruction. To minimize the effects of neighbor pattern averaging on spatial resolution, the background was also applied to the original patterns as well. If the confidence indexing (CI) was above 0.1 the original patterns were used for indexing, and if the CI was below 0.1 the neighbor pattern average was used for indexing. The deformed EBSD scans are presented with no reconstruction, and only CI standardization and CI thresholding of 0.1 are utilized, while the annealed microstructures had a grain dilation cleanup applied, changing less than 1% of the pixels. When extracting the grain size and shape statistics of the deformed material, a minimum grain size of 300 nm and a grain dilation cleanup were used for reconstruction parameters.

3. Experimental results

3.1. Layer refinement

Fig. 3 shows typical SEM secondary electron micrographs of the laminate cross-section after the third pass. The Mg alloy and Nb (light phase) layers are continuous, and the bonded interfaces have a wavy morphology. From integrating the thickness of each phase over the micrograph and considering the initial material, the Mg alloy and Nb phases appear to accommodate similar levels of strain, but the strain in Nb evidently is slightly more inhomogeneous since the variation in the Nb layer thickness is larger than that in the Mg layer thickness. The layer statistics for Mg–4Li/Nb and Mg–5Li/Nb are summarized in Table 2. The mean layer thickness for Mg–4Li is 217.8μm and for Mg–5Li is 204.6μm. This result is the first time such a fine layer thickness of ~200μm has been achieved for an Mg alloy/Nb laminate made by ARB.

3.2. Comparison of Mg–4Li and Mg–5Li processing paths

Fig. 4 compares the ARB 3 as rolled textures for Mg–4Li, Mg–5Li, and Nb. These textures are very similar. The same fiber development is present for Nb, and both Mg–4Li and Mg–5Li exhibit the similar texture features. Indeed, we found the heat treatment of 200°C for 1 h produced similar microstructures as in Fig. 5; deformed microstructures of Mg–4Li and Mg–5Li are similar; and the starting material, ARB 1, ARB 2, and ARB 3 in the Mg–5Li material exhibited a similar deformation texture. The Mg–4Li/Nb laminate exhibits more texture evolution over the ARB process, presumably due to the rolled texture used to initialize the Mg–5Li ARB process versus the hot extruded texture used to initialize the Mg–4Li ARB. Based off these observations and opportunity to cast the evolution of texture in the Mg–4Li in the context of literature (Risse et al., 2017; Zecevic et al., 2018a), we have chosen to focus on the presentation and characterization of Mg–4Li/Nb laminate.

3.3. Microstructural characterization

To gain information on the texture, grain size, and morphology, EBSD analysis was performed on TD sections of the Mg–4Li/Nb

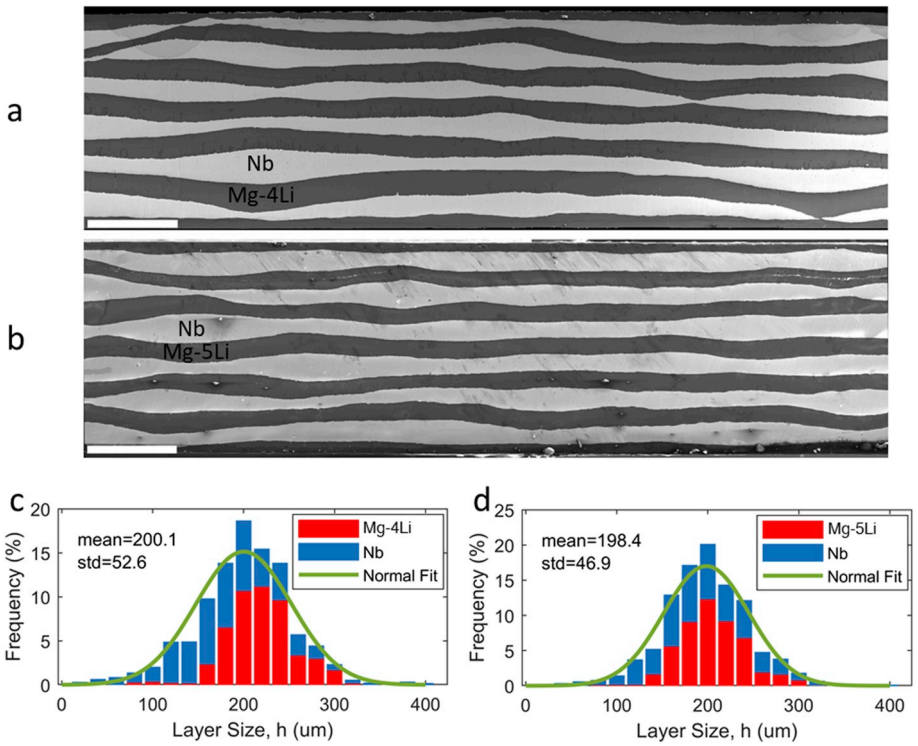

Fig. 3. SEM secondary electron micrographs in the RD/ND plane showing the layer morphology of the (a) Mg–4Li/Nb and (b) Mg–5Li/Nb laminate made by ARB. The light phase is Nb. Layer widths of (a) and (b) are summarized in (c) and (d). The scale bar is 1 mm. The pixel size and width of view field are identical between the two images.

Table 2
Summary of Mg–4Li, Mg–5Li, and Nb layer thicknesses after the third roll-bonding step along with their combined distributions as presented in Fig. 3. Results are reported as the mean and standard deviation of the fitted normal distributions. The distributions were constructed by extracting layer size along column of pixels in Fig. 3a and b. The process was repeated for each column of pixels along rolling direction (RD) and the count statistics fit assuming a normal distribution.

	Mg–4Li	Mg–5Li
Mg alloy layer size, h_{Mg} (μm)	217.8 ± 38.0	204.6 ± 35.9
Nb layer size, h_{Nb} (μm)	182.3 ± 58.8	192.1 ± 55.0
Mean layer size, h (μm)	200.1 ± 52.6	198.4 ± 46.9

Table 3
Twin boundary fraction for the pre-strained and ARB 3 specimens. The misorientation tolerance for the identification was set to 5°.

Twin Type	Label	Misorientation angle/axis	Twin boundary fraction (pre-strained)	Twin boundary fraction (ARB 3)
$\{10\bar{1}2\}$	TTW	86° < $1\bar{2}10$ >	5.9%	10.6%
$\{10\bar{1}1\}$	CTW	56° < $1\bar{2}10$ >	5.3%	5.1%
$\{10\bar{1}1\}$–$\{10\bar{1}2\}$	DTW 1	38° < $1\bar{2}10$>	17.0%	2.6%
$\{10\bar{1}1\}$–$\{10\bar{1}2\}$	DTW 2	30.1° < $1\bar{2}10$>	10.3%	5.8%

and Mg–5Li/Nb layered material after each roll bonding pass and after each annealing step (Table 1). Fig. 5 presents select EBSD scans for the annealed microstructures of Mg–4Li/Nb, wherein the inverse pole figure (IPF) corresponds to the ND. The Mg–5Li/Nb layered material showed similar microstructure and texture evolution and thus in the interest of space, data on Mg–5Li/Nb results are not shown.

Unlike the microstructure after rolling, we observe that the annealing steps result in Mg grains being slightly elongated and relatively homogeneous in orientation and size. The average equivalent circle grain size after each ARB cycle was approximately 3.8 μm, and after each annealing step was 9 μm. The major axis of the grains was mostly aligned with the rolling direction and the

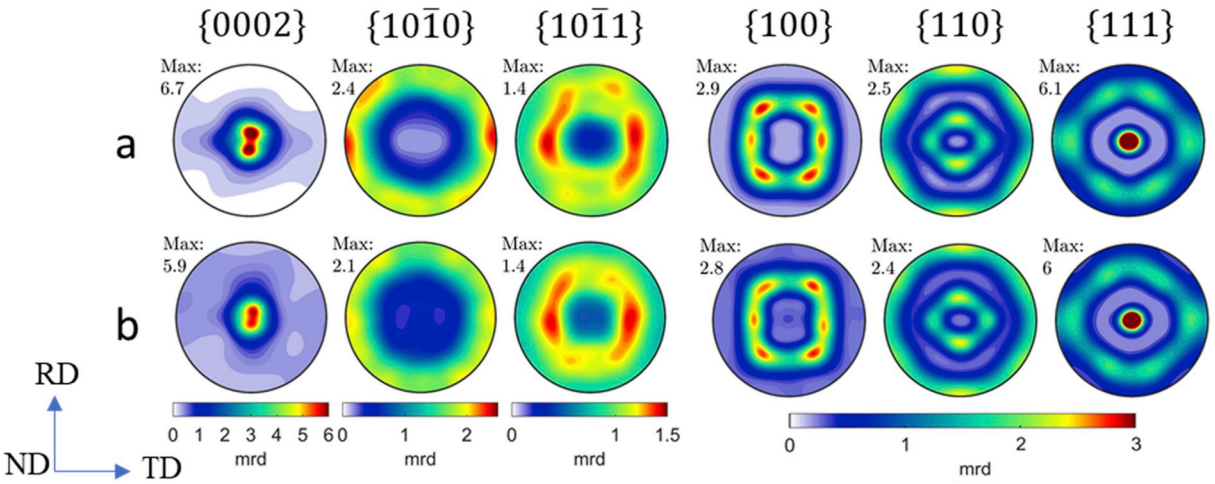

Fig. 4. Comparison of neutron diffraction textures for ARB 3 of the (a) Mg–4Li/Nb and (b) Mg–5Li/Nb laminates.

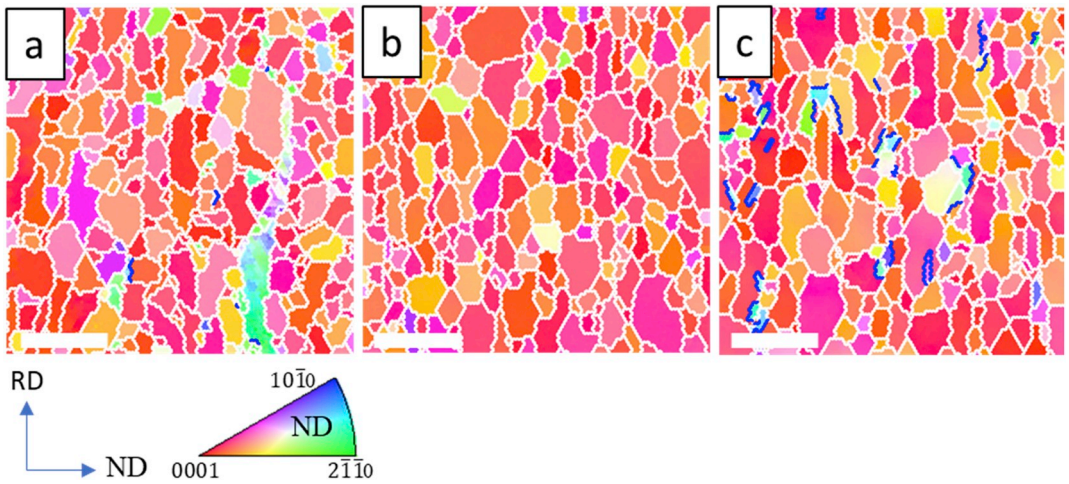

Fig. 5. Annealed microstructure of Mg–4Li after (a) 1 ARB cycles, (b) 2 ARB cycles, and (c) after 3 ARB cycles. White grain and blue $\{10\bar{1}2\} < \bar{1}011 >$ tensile twin boundaries are overlaid on the EBSD inverse pole figure map. The mean grain diameter by area is $8.5 \pm 3.7\mu$m, $9.3 \pm 3.5\mu$m, and $9.4 \pm 3.7\mu$m for (a–c) respectively. The recrystallized microstructure is relatively homogenous after annealing at 200°C for 1 h with most grains being represented by a **c**-axis distribution about the ND direction. The micron bar is 25μm, and the view fields are 100μm respectively. (For interpretation of the references to colour in this figure legend, the reader is referred to the Web version of this article.)

average through thickness grain size after ARB was 2 μm. The annealing step "resets" the grain shape after rolling, resulting in an aspect ratio change of RD: ND = 3.5 : 1 to RD: ND = 2.5 : 1. Consequently, with intermediate annealing the grain shape in the Mg phase at the end of each pass is determined by the amount of strain imposed by the ARB pass and fragmentation of grains rather than the total accumulated strain after all the passes. Interestingly, low volume fractions of deformation tensile twins$\{10\bar{1}2\} < \bar{1}011 >$ are observed for the annealed ARB 3 case in Fig. 5c. We speculate that these twins are an artifact of interface constraint on the Mg–4Li phase and its ability to fully relax during cooling (Lesuer et al., 1996).

To determine the number of grains that span a layer, we used the EBSD maps of the annealed microstructure in Fig. 5 combined with the mean layer statistics presented in Table 2. We observe that the number of Mg grains that span a layer after an annealing step reduces with layer thickness from ~140 for the ARB 1 sample, ~60 for the ARB 2 sample, and ~20 for the ARB 3 sample. Thus, even after the third pass the individual layers are still polycrystalline.

The EBSD maps also indicate significant texture evolution from the initial texture and are in agreement with neutron results. The textures exhibited some features that are not commonly found in classical rolling textures of BCC and HCP polycrystalline materials. In the Nb phase, we observe a strong γ-fiber, but the α-fiber is unusually weak after such a large rolling strain. A thorough texture analysis requires many more grains than contained in these EBSD maps. For this reason, we later analyze texture in more detail based on measurements from neutron diffraction.

With EBSD we can further investigate the inhomogeneous deformation. Presented in Fig. 6 are maps of the deformed Nb microstructures; it is clear the grains are no longer uniform in orientation. A closer examination shows that within each grain,

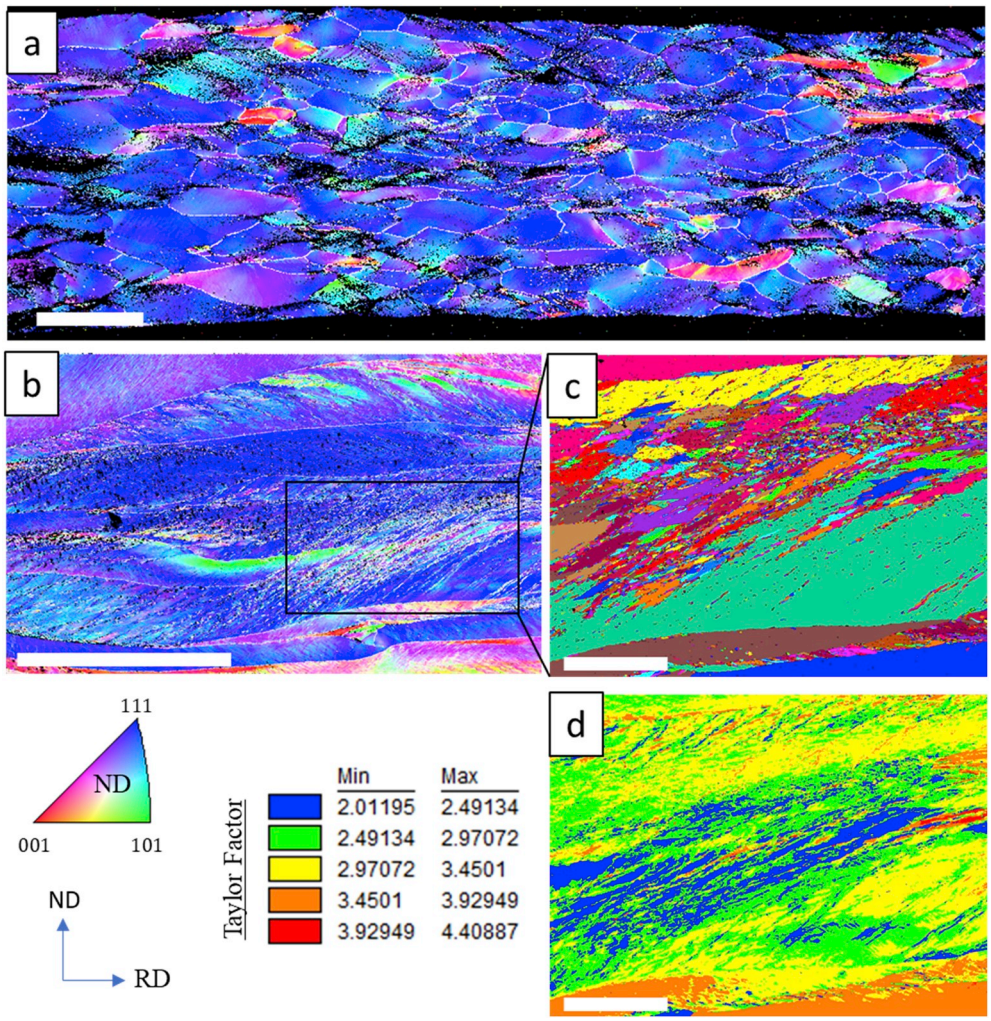

Fig. 6. Nb EBSD inverse pole figure maps for (a) ARB 1 and (b) ARB 2 with misorientation greater than 15° denoted by white lines. Black points are unindexed. Unique grain map of the shear band (c) showing the formation of very fine grains inside the highly elongated macro-grains. (d) Taylor factor map. The micron bars are 400μm and 200μm in (a,b), and 50μm in (c,d) respectively.

orientation gradients can be significant, particularly in the larger grains. We find that the Nb deformation was relatively inhomogeneous compared to Mg–4Li/Mg–5Li. Within the Nb grains, it appears that some deformation bands have formed. Deformation bands can be characterized by their lamella shape and intense shear and reorientation. These are one of the possible origins of the observed variation in thickness of Nb layers. The texture of the Nb phase, when encompassing many grains, exhibits a common rolling texture. In contrast, the texture of Nb only considering locally the region around the shear bands is indicative of a characteristic shear texture.

To investigate the origin of the deformation bands, we generated a map of the Taylor factor for each pixel in the EBSD image. The Taylor factor plot of the deformation band in Fig. 6d shows significant softening. Evidently, the deformation bands are reorienting the relatively finer grains to lower Taylor factors, an indication of localized geometric softening, which is usually accompanied by plastic instabilities (Bhattacharyya et al., 2015; Dillamore et al., 1979; Knezevic et al., 2014b, 2015; Knezevic and Kalidindi, 2007; Nguyen-Minh et al., 2015).

Fig. 7 shows the microstructure for the Mg phase after pre-straining and after ARB 3. The pre-strained sample has about half of the applied strain of the ARB 3 sample and a larger initial grain size of approximately 38 μm (Risse et al., 2017). In both cases, heterogenous deformed microstructures are observed. At the top of Fig. 7c there is also a clear rotation of the grain alignment away from RD that corresponds to the rotation of the Mg layer due to a shear instability and rotation of the Nb phase. As mentioned earlier, the mean aspect ratios RD: ND are 2.5 : 1 and 3.5 : 1 before and after each ARB pass, respectively for the Mg phase. No significant change was observed from pass to pass. In Fig. 7c there are also several highly elongated grains. These elongated grains are expected given the distribution of initial aspect ratios and the applied strain.

Dynamic recrystallization in severely rolled Mg and its alloys has been reported, but generally at elevated temperature (Al-Samman and Gottstein, 2008; Barrett et al., 2017; Ghorbanpour et al., 2019a, b; Jahedi et al., 2018a). Here we used EBSD to examine

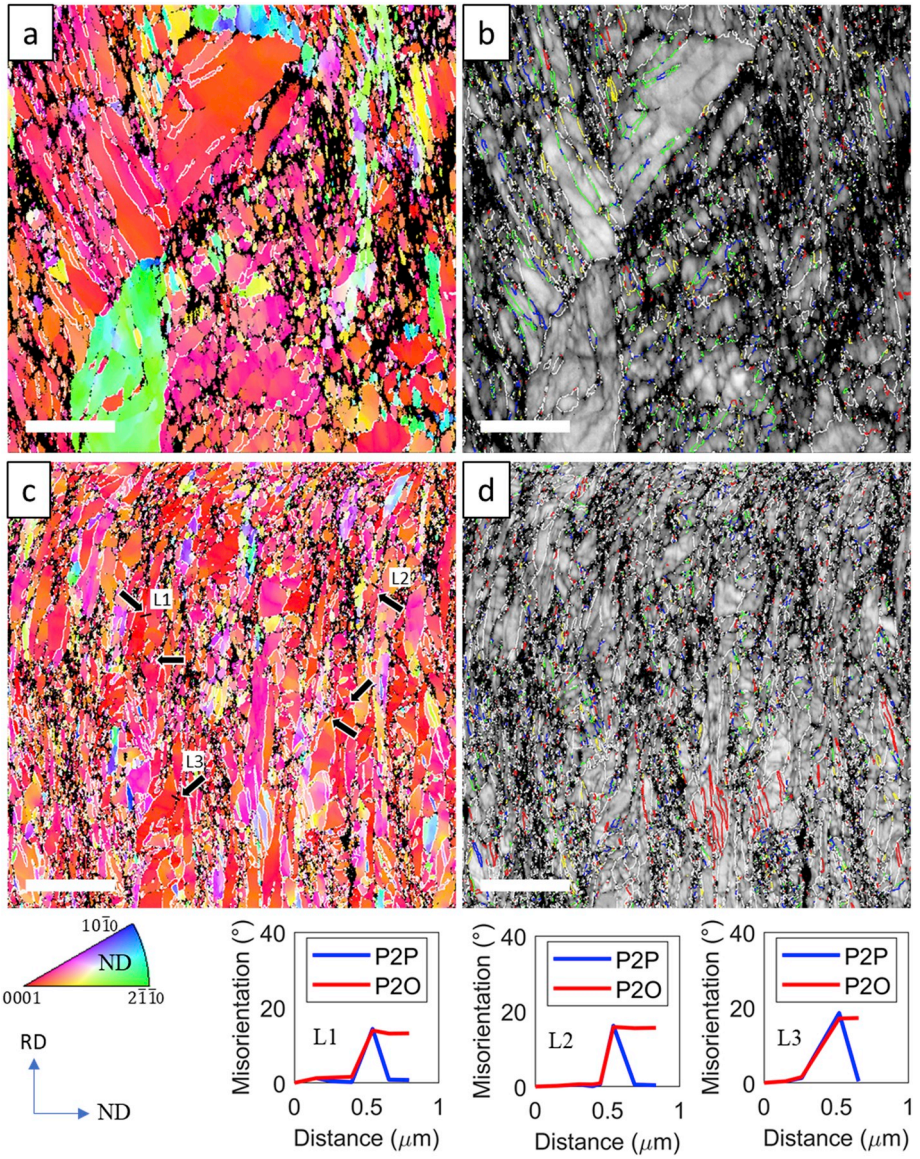

Figure 7. (a, c) Pre-strained and ARB 3 as rolled ND IPF maps. (b, d) Pre-strained and ARB 3 as rolled image quality maps. White boundaries are misorientations greater than 15°. The twin boundaries as defined in Table 3 are TTW boundaries = red, CTW = yellow, type 1 DTW = green, and type 2 DTW = blue. Black points are unindexed. The scale bar is 20μm and the view field 100μm. Line scans are shown to highlight unenclosed high angle boundaries that indicate continuous dynamic recrystallization as one mechanism of fragmentation. (a) has the signature of this with small grain decorating large grains. P2P is point-to-point and P2O is point-to-origin which describes the misorientation that is being measured in the misorientation line scan.

both the Mg phase and Nb phase for dynamic recrystallization. Fig. 7 shows the EBSD maps of the pre-strained and ARB 3 as-rolled material. For the Mg phase, we observe small grains decorating the larger grains and the presence of unenclosed grain boundaries, suggesting continuous dynamic recrystallization as one mechanism of fragmentation. Examples of unenclosed grain boundaries with misorientation greater than 15° are given as misorientation line profiles at the bottom of Fig. 7. For the Nb, microstructure analysis reveals that fine grains tend to nucleate in shear bands. However, many of the grains exhibit misorientation that spans the IPF legend, and the boundaries of the original grain remain intact. We additionally observe that the rolling texture of the Nb phase does not contain classic recrystallization components. It is expected that upon recrystallization the γ-fibre would develop strong $\{11\bar{1}\} < 112 >$ components, and this change was not observed in the Nb phase. Further, analysis of the misorientation and EBSD scans did not show any marked changes before and after annealing that would suggest static recrystallization.

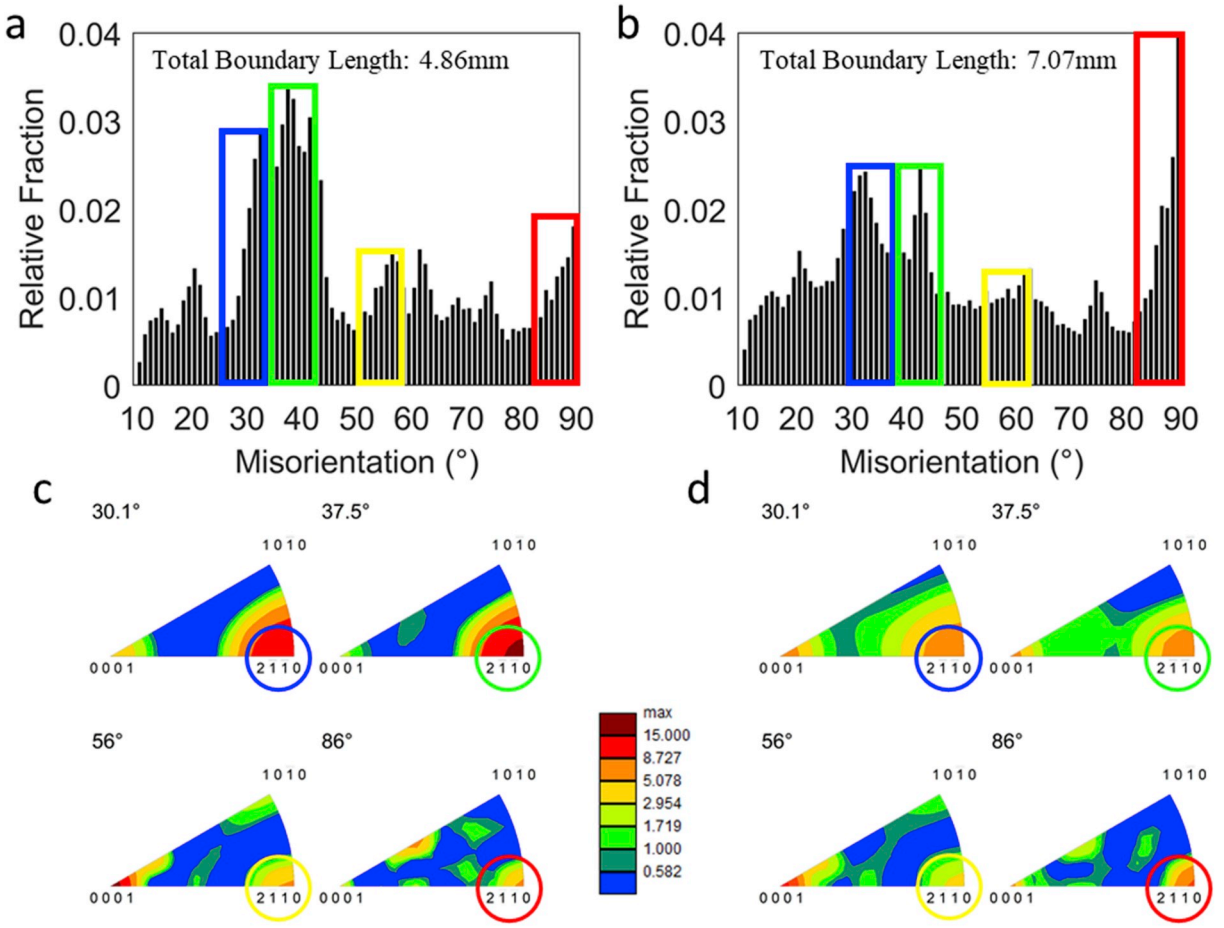

Fig. 8. Axis angle disorientation (a, b) and correlated grain boundary axis angle textures (c, d) between identified grains for (a, c) Pre-strained and (b, d) ARB 3 as rolled. The twin types as defined in Table 3 are TTW = red, CTW = yellow, type 1 DTW = green, and type 2 DTW = blue. Analysis was performed on the 100 × 100μm view fields shown in Fig. 7. (For interpretation of the references to colour in this figure legend, the reader is referred to the Web version of this article.)

3.4. Deformation twinning

In general, it is well known that Mg and their alloys tend to deformation twin easily (Jahedi et al., 2017c, 2018b; Kelly and Hosford, 1968; Knezevic et al., 2016b). As previously mentioned, $\{10\bar{1}2\} < \bar{1}011 >$ extension twinning is expected occurred in small amounts and it is not expected to be a dominate deformation mechanism for Mg–4Li (Risse et al., 2017). To determine whether twinning occurred in the present Mg–4Li/Nb laminates, we employed EBSD and characteristic matrix/twin disorientation boundary recognition for the common Mg twins $\{10\bar{1}2\} < \bar{1}011 >$ extension twins and $\{10\bar{1}1\} < 10\bar{1}\bar{2} >$ type contraction twins, as well as some $\{10\bar{1}1\} < 10\bar{1}\bar{2} >$ /$\{10\bar{1}2\} < \bar{1}011 >$ double twins. Fig. 7 shows the EBSD map of the ARB 3 sample with the twin/matrix boundaries highlighted. During the processing of these samples, deformation twinning was detected but found to not be profuse. Fig. 7 presents a higher resolution EBSD map of the Mg–4Li phase in the ARB 3 sample, in which some very fine $\{10\bar{1}2\} < \bar{1}011 >$ extension and $\{10\bar{1}1\} < 10\bar{1}\bar{2} >$ contraction type twins are highlighted along with some double twins. To assess changes in twinning for each type of twin, Fig. 8 compares the axis/angle disorientation distributions and correlated grain boundary axis/angle textures in the pre-strained and ARB 3 as-rolled sample. Table 3 summarizes the changes in the twin boundary fraction from the pre-strained material to the final ARB 3 step. The results indicate that during ARB, $\{10\bar{1}2\} < \bar{1}011 >$ extension twinning occurred more than other twinning modes. The corresponding twin area fractions for these extension and contraction twins were not quantified, but their contribution given the fine grain size appears to be minimal. We conclude that over a large strain period of 2.45, that deformation twinning was not a predominant deformation mechanism during ARB.

3.5. Texture evolution

The analysis thus far indicates substantial changes in the microstructure and texture after each rolling pass and annealing step. While the EBSD examination provides local texture information, we used neutron diffraction to obtain bulk textures. Fig. 9 presents

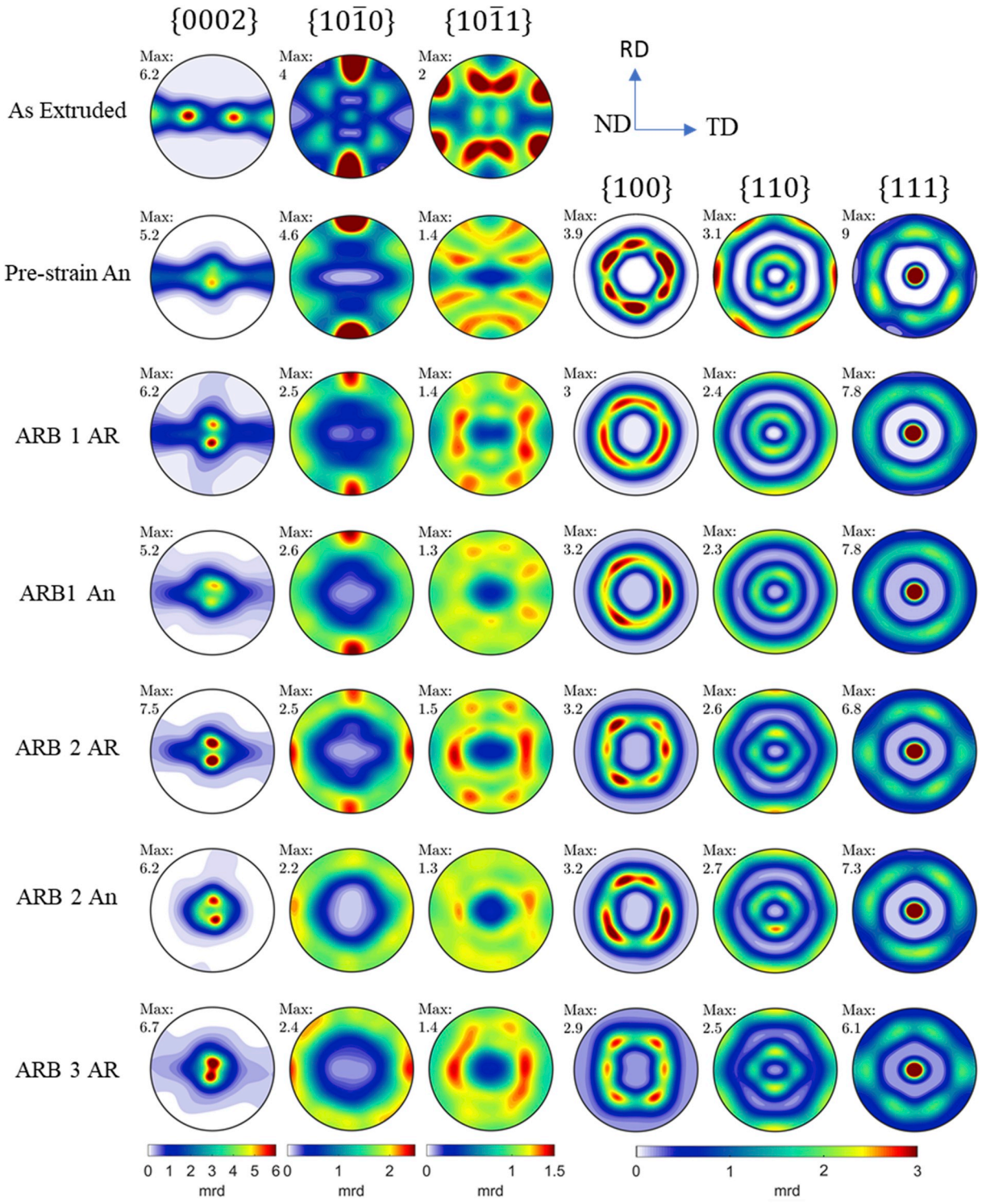

Fig. 9. Textures for Mg–4Li and Nb in Mg–4Li/Nb composites. All pole figures are derived from neutron diffraction except for the 'Pre-strain An Nb' pole figure, which was obtained from EBSD.

the Mg and Nb textures for the Mg–4Li/Nb ARB, as measured from neutron diffraction, after each processing step, including relevant as deformed and annealed textures for the starting material, pre-strained, and ARB rolling passes. In each case, three pole figures are used to display the textures: the basal {0002}, prismatic{10$\bar{1}$0}, and pyramidal{10$\bar{1}$1} poles for Mg and the {100}, {110}, and {111} poles for Nb. Not shown are the textures for the Mg–5Li/Nb laminate in the interest of space. After three ARB cycles both Mg–4Li and

Mg–5Li phases have similar textures; despite Mg–4Li/Nb starting with an extrusion texture and the Mg–5Li/Nb starting with a rolling texture.

The Mg textures are observed to undergo significant evolution (more so than Nb). First, we see that the Mg–4Li textures in the as-rolled state are similar to those of the Mg–4Li material when rolled alone, as reported in (Zecevic et al., 2018a). This similarity arises because many grains span the layer thickness and there is not a significant influence of the Mg/Nb interface on plastic deformation. This also suggests that the co-deformation of the composite made by rolling Mg–4Li and Nb together does not likely play a role in the Mg texture. From the {0002} pole figures, it is seen that the basal poles split about the ND in the RD after rolling. Early Mg texture analysis of pure, rolled HCP material such as Zn or Cd, attribute this type of split to slip geometry present when the c/a ratio is larger than ideal (Wang and Huang, 2003). Rietveld analysis of the neutron diffraction spectrum reveals a c/a ratio slightly less than ideal, and the split behavior should be understood as an artifact of the Li influence on slip behavior (Agnew et al., 2001). Annealing weakens the Mg–4Li textures in all cases, but there is an increase in **c**-axis alignment after the second ARB pass. Interestingly, it takes several ARB and annealing cycles for the $\{10\bar{1}0\}$ alignment of the extrusion texture with RD to disappear and a pure rolling texture to form. In the final step, a strong basal texture is present where the peak split towards RD collapses and becomes more aligned along the ND. The intensities and texture components do not change significantly by the third pass, and thus the Mg phase appears to achieve a steady state after two passes. The interpretation of this peak collapse and the contribution of slip, fragmentation, and twinning will be addressed in the modeling section.

The Nb phase maintains a strong texture after each rolling pass and evolves in a similar manner for the Mg–4Li and Mg–5Li cases. The important observation is a gradual evolution of a strong ND||<111> γ-fiber that evolves from $\{111\}\langle 11\bar{2}\rangle$ to $\{111\}\langle 1\bar{1}0\rangle$ components and the resulting slow development of the α-fiber. The Nb phase deformation texture was unaffected by annealing, which is not surprising since annealing was carried out at 8% of the melting temperature of Nb, and the variation in the AR and AN Nb textures is attributed to measured variation in strain between samples taken for neutron analysis.

To better display the development of individual texture fibers, the $\varphi_2 = 45^\circ$ ODF sections are shown in Fig. 10. While the texture evolution is not classically reported in literature for cold rolled Nb such as (Knezevic and Bhattacharyya, 2017; Knezevic and Landry, 2015; Raabe and Lücke, 1994a; Raabe and Luecke, 1994b), the strong γ-fiber in the initial texture is also not a common initial texture in these studies, and larger strain is achieved during the ARB process. Compared to previous ARB systems which had nearly identical initial texture, purity, and microstructure, the evolution of Nb is very similar to unannealed coarse layered Cu/Nb (Carpenter et al., 2014), which had the same γ-fiber and α-fiber development. In stark contrast, intermediately annealed Zr/Nb (Knezevic et al., 2014c) and Cu/Nb (Carpenter et al., 2012) developed a much weaker γ-fiber with a significant fraction of the $\{001\}\langle 1\bar{1}0\rangle$ component on the α-fiber. These observations suggest that the 200°C intermediate anneals do not substantially affect the Nb texture evolution. The contribution of slip modes and microstructure associated with the evolution of the strong γ-fiber will be investigated in what follows with crystal plasticity modeling.

3.6. Hardness evolution

The hardness evolution of the Mg and Nb phases can be used as an indication of whether the layers are expected to co-deform or break up due to shear instabilities. To determine the amount of strengthening arising from the deformation of each rolling pass, the hardness of the individual phases after rolling and annealing were measured. Fig. 11 presents the results from the Knoop hardness testing for the Mg–4Li material. The hardness of the Mg phase does not change substantially from pass to pass, a result of the intermediate annealing effectively resetting the microstructure. Identical hardening and softening behavior and magnitudes were observed in the Mg–5Li material. The annealing temperature of 200 °C, however, is far below the Nb melting temperature. The Nb hardness increases through ARB 2, after which the Nb hardness saturates. The Nb strength in the annealed specimens were also measured for completeness. The hardness of Nb was unaffected by the static annealing step between passes.

The small variations in the Knoop hardness (KH) for the as-rolled and anneal Mg–4Li is within a standard deviation of its neighbors, with the exception of ARB 1 as rolled. The Knoop measurements were collected on RD/ND cross-sections, and the textures shown in Fig. 6 reveal distinct realignment of the prismatic planes from RD to TD in ARB 2 and ARB 3. Several contributing factors prevent tying the strength change exclusively to texture, mainly: i) the stress under the indenter is complex, and ii) the first ARB case has only Mg–4Li on the outside, and in addition to having a smaller rolling reduction, would have potentially higher shear strain compared with ARB 2 and ARB 3. Given the lack of evolution of the γ-fiber in Fig. 10 the strength of Nb appears to be governed by grain refinement, dislocation formation, and substructure formation.

The ARB 3 step had a starting strength differential (HK_{Nb}: HK_{Mg})of 3.75 and ending strength differential of 2.18. In comparison, the Zr/Nb material of (Carpenter et al., 2015a; Knezevic et al., 2014c), which was processed without layers breaking up, had a strength differential (HK_{Nb}: HK_{Zr})of 0.87 in the annealed state and 0.74 in the as-rolled state after four ARB cycles and a strain of 2.9. There is both a difference in the harder phase and in the work hardening amount of 41% for Mg–4Li vs 20% for Zr. The hardness of the Nb in the Zr/Nb multilayer was also not affected by the static anneal of 600 °C and had similar Knoop hardness to the Nb in the Mg–4Li/Nb.

The layer stability during the deformation processing of metal/metal composites was studied as a function of work hardening rate, strength differential, and reduction in (Yazar et al., 2005). The main finding of the study is that in the absence of work hardening, a strength differential greater than 2 and a reduction on the order of 50% will result in necking and breaking of the harder phase. Conversely, with sufficient work hardening, strength differentials as high as 5 times can still result in stable layer refinement, even at large strains. However, the study of (Yazar et al., 2005) only considered the same work hardening rate between phases and therefore more or less a single strength differential throughout the deformation process when the two phases are co-deforming. By ARB 3 the

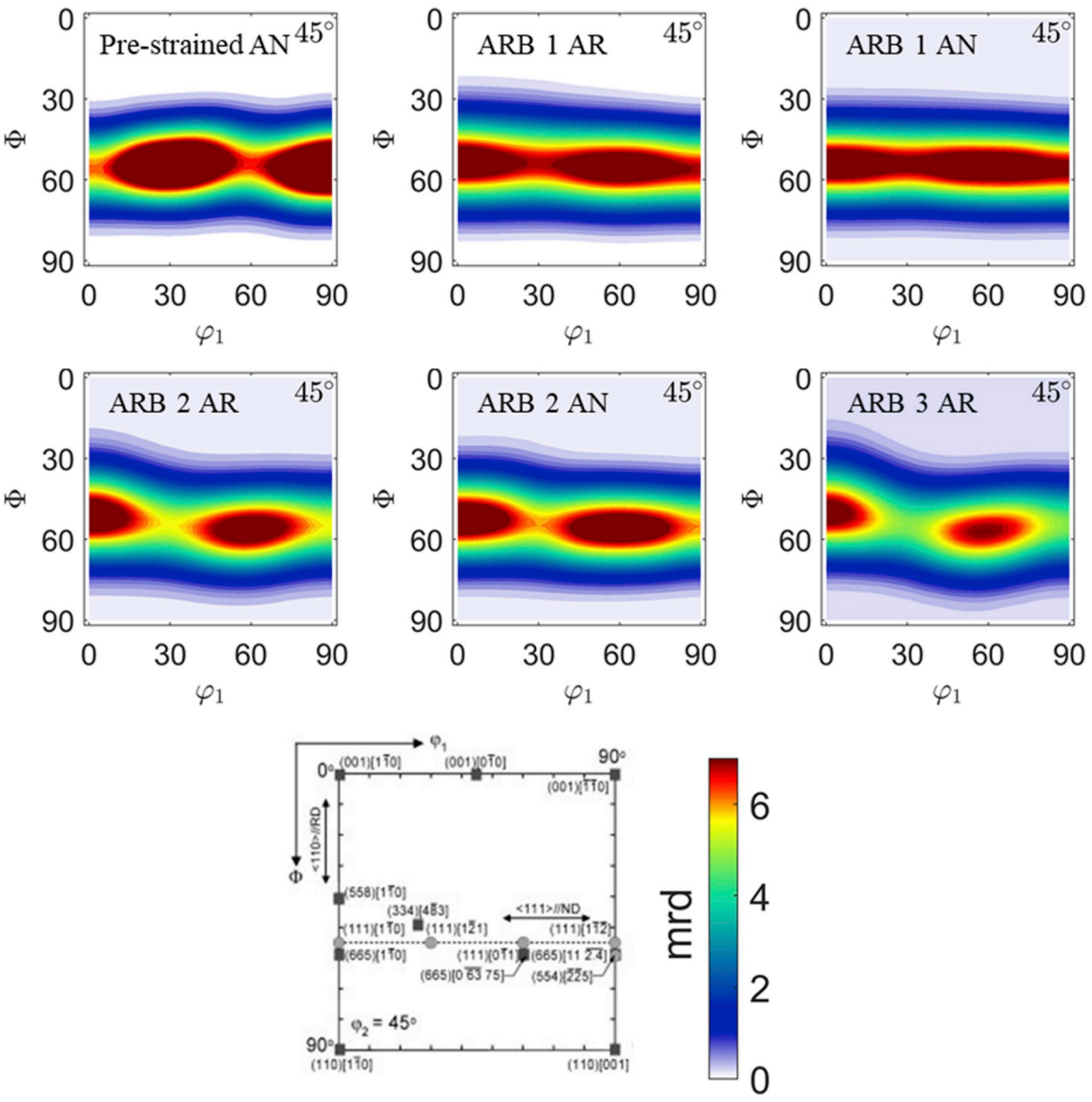

Fig. 10. Series of $\varphi_2 = 45°$ ODF sections showing the evolution of the γ ND||⟨111⟩ rolling fiber. ODF sections correspond to pole figures presented in Fig. 6, and important fibers and texture components in BCC metals are shown as a legend (N. Lee et al., 2015).

Nb phase has very little work hardening and the Mg phase still has significant work hardening and strength differentials are clearly a function of strain. This presents a different case than has been studied in literature, and it is not clear if the necking in the Nb phase observed in the third ARB pass is expected based on the reduction, hardening behavior, or strength differential. For practical purposes and given the constraints of the material properties and thermal treatments, future rolling should use the lowest rolling reduction that allows cutting and stacking of the ARB material.

4. Modeling methods

Achieving such fine-layered structures via severe plastic deformation offers the opportunity to study the deformation mechanisms in the large strain regime. It is clear from the microscopy that deformation twinning has a limited role during the rolling the Mg-xLi alloy after ARB and anneal cycles refine the microstructure. The texture evolution changes in both the Mg alloy and Nb phase suggest that deformation was accommodated by slip. Both phases are expected to deform by multiple slip families: the basal $< \mathbf{a} >$, prismatic $< \mathbf{a} >$, and pyramidal type I and type II $< \mathbf{c}+\mathbf{a} >$ slip families for the Mg-xLi (Zecevic et al., 2018a) and the $\{1\bar{1}0\} < 111 >$ and $\{11\bar{2}\} < 111 >$ slip families for the Nb (Ardeljan et al., 2016b; Knezevic et al., 2014a). However, it is not possible with the characterization techniques used here, EBSD or neutron diffraction, to determine which slip systems and families were active during deformation.

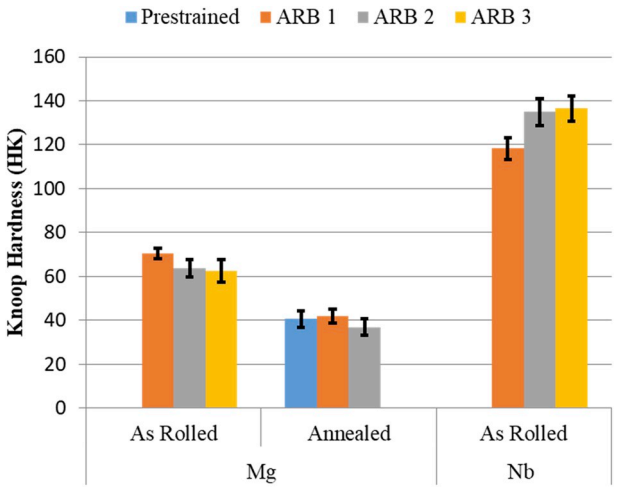

Fig. 11. Knoop hardness of individual layers for the Mg–4Li/Nb laminate.

In this section, we describe a multiscale polycrystalline modeling method, EPSC, and the dislocation density (DD) law used as a slip strength model, which we will apply to study texture evolution in each phase of this two-phase material system. The basic idea is that the DD-EPSC model predicts which slip systems must have been active in order to achieve the measured texture at the end of deformation, all while being constrained by the stress-strain curve. The EPSC model has been applied to many single-phase Mg alloys including the Mg–4Li of interest here (Risse et al., 2017). However, in these prior works, the texture evolution of Mg co-deforming with another metal has not been treated, and the ARB sequence has several interesting texture features, such as peak collapse and realignment of prismatic poles from RD to TD that were not observed in prior modeling work of single-phase Mg–4Li.

To elicit trends in slip activities, several important assumptions in addition to those intrinsic to EPSC are made: i) the rolling process can be approximated as plane strain, ii) the coupling of Mg–4Li and Nb at the interface does not affect grains far from the interface and the strength of intergranular interactions are governed by their respective polycrystal, iii) strain partition between phases is a secondary effect in texture evolution at large strain, and iv) the continuous dynamic recrystallization observed experimentally does not play a significant role in texture development other than softening the main rolling components and can omitted.

In the Mg–4Li/Nb composite application here, the anisotropy in the interaction between grains within the same phase needs to be considered due to the strong coupling of pyramidal slip and the effective medium for this particular rolling texture, and due to the strong stability the initial gamma fiber in Nb. The RDC scheme is used less often than standard EPSC and to the authors' knowledge has not been applied to calculating the texture evolution during rolling of metal/metal laminates. Besides the utility of the RDC method for this study, we find the use of RDC attractive because the differences in the deformation behavior of the phases and in particular deformation regions (Takajo et al., 2019), such as interfaces, can be simulated in FE-EPSC forming operations. For these reasons, we briefly review the RDC scheme in the description below.

4.1. Review of the EPSC crystal plasticity

The EPSC model formulation was originally developed in (Turner and Tomé, 1994) and extended later in (Barrett and Knezevic, 2019; Ghorbanpour et al., 2017; Zecevic et al., 2015, 2017a; Zecevic and Knezevic, 2017, 2019). In EPSC the grains and polycrystal deform by elastic deformation and plasticity via deformation twinning and crystallographic slip. The latter uses crystal plasticity, wherein slip and twinning occur on specified crystallographic systems. EPSC can predict the relationships between crystallographic texture evolution, effective stress-strain response, and the activity of the various slip/twin systems used by each grain in the polycrystal.

We adopt the following notation in our description of EPSC. The symbol "•" signifies a dot product and "⊗"a tensor product. A family of slip systems is denoted by α, and individual slip systems belonging to the family are denoted by s.

In EPSC, a polycrystal is represented by a group of grains with a given lattice orientation, ellipsoidal shape, and volume fraction. The solution procedure is based on an equivalent inclusion method where each grain is treated as an ellipsoidal inclusion inside the homogeneous equivalent medium (HEM). The stress and strain rates of the inclusion are solved using a Green's function approach. The HEM represents the surrounding polycrystal, and as the name "self-consistent" indicates, has a tangent stiffness that is determined by enforcing the macroscopic stress and strain rate to be volume averages of the corresponding single crystal quantities, i.e.,

$$\hat{\boldsymbol{\sigma}} = \langle \hat{\boldsymbol{\sigma}}^c \rangle; \quad \dot{\boldsymbol{\varepsilon}} = \langle \dot{\boldsymbol{\varepsilon}}^c \rangle. \tag{1}$$

In Eq. (1), the polycrystal Jaumann stress rate and strain rate are expressed as the volume average of the corresponding grain, c, quantities. These macroscopic quantities are linked using the following:

$$\hat{\boldsymbol{\sigma}} = \mathbf{L}\dot{\boldsymbol{\varepsilon}}, \tag{2}$$

where $\mathbf{L}$ is the instantaneous elasto-plastic stiffness tensor that is calculated iteratively using the self-consistent (SC) procedure (Eshelby, 1957; Turner and Tomé, 1994). The Cauchy stress rate is related to the Jaumann stress rate according to the following relation (Zecevic et al., 2017a):

$$\dot{\boldsymbol{\sigma}} = \hat{\boldsymbol{\sigma}} + <\mathbf{W}^c\boldsymbol{\sigma}^c> - <\boldsymbol{\sigma}^c\mathbf{W}^c> = \mathbf{L}\dot{\boldsymbol{\varepsilon}} + <\mathbf{W}^c\boldsymbol{\sigma}^c> - <\boldsymbol{\sigma}^c\mathbf{W}^c>, \tag{3}$$

where $\mathbf{W}^c$ is an elastic spin per grain, *c,* which will be defined shortly. Equation (3) is integrated over straining time explicitly for obtaining the macroscopic Cauchy stress. The local strain rate per crystal, *c*, and the overall strain rate are related by the localization tensor, i.e.,

$$\dot{\boldsymbol{\varepsilon}}^c = \mathbf{A}^c\dot{\boldsymbol{\varepsilon}} \tag{4}$$

The localization tensor for a given instantaneous local elasto-plastic stiffness $\mathbf{L}^c$ is

$$\mathbf{A}^c = \left(\mathbf{L}^c + \mathbf{L}^{c^*}\right)^{-1}\left(\mathbf{L}^{c^*} + \mathbf{L}\right), \tag{5a}$$

where

$$\mathbf{L}^{c^*} = M^{eff}\mathbf{L}(\mathbf{S}^{c-1} - \mathbf{I}) \tag{5b}$$

is the effective stiffness defined by the interaction equation below,

$$(\hat{\boldsymbol{\sigma}}^c - \hat{\boldsymbol{\sigma}}) = -\mathbf{L}^{c^*}(\dot{\boldsymbol{\varepsilon}}^c - \dot{\boldsymbol{\varepsilon}}). \tag{6}$$

and where $\mathbf{S}^c$ is the symmetric portion of the Eshelby tensor and $\mathbf{I}$ is the fourth-rank identity tensor. The parameter M^{eff} in the interaction equation (5b) reflects the degree of coupling between the grain and the HEM. Finally, the above relations result in an implicit equation for macroscopic (matrix) tangent stiffness,

$$\mathbf{L} = <\mathbf{L}^c\mathbf{A}^c><\mathbf{A}^c>^{-1}. \tag{7}$$

At the grain/local level, the constitutive relation is given by

$$\hat{\boldsymbol{\sigma}}^c = \mathbf{C}^c\left(\dot{\boldsymbol{\varepsilon}}^c - \sum_s \mathbf{m}^{c,s}\dot{\gamma}^{c,s}\right) - \boldsymbol{\sigma}^c tr(\dot{\boldsymbol{\varepsilon}}^c), \tag{8}$$

where $\mathbf{C}^c$ is the fourth rank elastic stiffness tensor, $\sum_s \mathbf{m}^{c,s}\dot{\gamma}^{c,s}$ is the plastic strain rate made up of slip system shearing rates, $\dot{\gamma}^{c,s}$, and where the Schmid tensor is given by $\mathbf{m}^{c,s} = 0.5(\mathbf{b}^{c,s} \otimes \mathbf{n}^{c,s} + \mathbf{n}^{c,s} \otimes \mathbf{b}^{c,s})$, where $\mathbf{b}^{c,s}$ and $\mathbf{n}^{c,s}$ are the slip system direction and plane normal, respectively.

To activate slip system *s*, the net resolved stress accounting for the grain stresses and backstress, $\tau_{bs}^{c,s}$, must reach the slip resistance, $\tau_c^{c,s}$, i.e.

$$\mathbf{m}^{c,s}\cdot\boldsymbol{\sigma}^c - \tau_{bs}^{c,s} = \tau_c^{c,s} \tag{9}$$

while the stress has to remain on the evolving crystal yield surface, i.e.,

$$\mathbf{m}^{c,s}\cdot\hat{\boldsymbol{\sigma}}^c - \dot{\tau}_{bs}^{c,s} = \dot{\tau}_c^{c,s}. \tag{10}$$

The slip resistance defines the single crystal yield surface. The addition, the backstress term introduces kinematic hardening effects at the slip-system level. Therefore, a single crystal yield surface expands with deformation as defined by $\tau_c^{c,s}$, and shifts as defined by $\tau_{bs}^{c,s}$.

The slip resistance and backstress evolve with the shearing rates using:

$$\dot{\tau}_c^{c,s} = \sum_{s'} h^{ss'}\dot{\gamma}^{c,s'}, \tag{11}$$

$$\dot{\tau}_{bs}^{c,s} = \sum_{s'} h_{bs}^{ss'}\dot{\gamma}^{c,s'}, \tag{12}$$

where $h^{ss'}$ and $h_{bs}^{ss'}$ are the hardening matrix and the backstress matrix, respectively. The components of these matrices depend on the hardening and backstress evolution laws used, which are defined in the appendices.

Finally, the crystal constitutive law is expressed as

$$\hat{\boldsymbol{\sigma}}^c = \mathbf{L}^c\dot{\boldsymbol{\varepsilon}}^c, \tag{13}$$

where $\mathbf{L}^c$ is:

$$\mathbf{L}^c = \mathbf{C}^c - \mathbf{C}^c\sum_s \mathbf{m}^{c,s} \otimes \left(\sum_{s'}\left(X^{ss'}\right)^{-1}\mathbf{m}^{c,s'}(\mathbf{C}^c - \boldsymbol{\sigma}^c \otimes \mathbf{i})\right) - \boldsymbol{\sigma}^c \otimes \mathbf{i} \tag{14}$$

and where

$$X^{ss'} = h^{ss'} + h_{bs}^{ss'} + \mathbf{C}^c\cdot\mathbf{m}^{c,s} \otimes \mathbf{m}^{c,s} \tag{15}$$

Note that indices *s* and *s'* in Eqs. (14) and (15) span the active slip systems. Therefore, while full hardening and backstress matrices

are used for updating slip resistance and backstress, only a portion of them is used for the calculation of tangent stiffness.

The grain spin tensor necessary for texture evolution, $\mathbf{W}^c$, is:

$$\mathbf{W}^c = \mathbf{W}^{app} + \mathbf{\Pi}^c - \mathbf{W}^{p,c}, \tag{16}$$

where $\mathbf{W}^{app}$ is the applied spin, $\mathbf{\Pi}^c$ is the spin calculated from an applied macroscopic strain rate to the polycrystal and the anti-symmetric part of the Eshelby tensor for grain c (Lebensohn and Tomé, 1993), and $\mathbf{W}^{p,c}$ is the plastic spin. The plastic spin is:

$$\mathbf{W}^{p,c} = \sum_s \mathbf{q}^{c,s}\dot{\gamma}^{c,s}, \tag{17}$$

where $\mathbf{q}^{c,s} = 0.5(\mathbf{b}^{c,s} \otimes \mathbf{n}^{c,s} - \mathbf{n}^{c,s} \otimes \mathbf{b}^{c,s})$.

4.2. Relative directional compliance (RDC)

SC models are based on an interaction equation that links the deviations in the grain and HEM to the deviations in the grain and HEM strain rates. The general form for the interaction equation Eq. (5) introduces a parameter M^{eff} that can be associated with the strength of the coupling between the grain and the homogeneous medium. The values are usually associated with the tangent stiffness $M^{eff} = 0.1$or secant stiffness $M^{eff} = 1$. In conjunction with these values, it is common in EPSC calculations to use the same M^{eff} for all grains in the polycrystal at all time (or strain) steps. However, in some deformation conditions, particularly at severe straining such as the present situation, the texture can adopt hard and very soft orientations and a single value of M^{eff} may not apply. Additionally, in the case of a composites where each phase exhibits different slip behavior, a single value for M^{eff} is not able to describe the interactions in both phases.

Here we adopt the RDC scheme to determine the M^{eff} value to use in every time step and for each phase (Tomé, 1999). In each time step, the tangent approach is used to determine the RDC for every grain, and the grains with the lowest and the highest value are determined. RDC for each grain is calculated as the ratio of the norms of the directional compliance of the grain and of the medium. The grain with the maximum RDC is assigned a value of $M^{eff} = 1$ and the minimum RDC a value of $M^{eff} = 0.1$. An interpolation scheme between these two values is used to determine the value of M^{eff} assigned to the rest of the grains and the self-consistent calculations are repeated for the strain increment. A value of M^{eff} near 0.1 would represent highly directional interaction, whereas $M^{eff} = 1$ would correspond to the full constraints Taylor model, in which there is no directionality in the grain and HEM interaction.

4.3. Review of the dislocation density-based hardening law

The EPSC model requires as input a hardening law that governs the evolution of slip strength as a function of deformation. For this, we use a dislocation density based law that was developed for pure HCP metals (Zr, Mg) and has been extended to alloys and metals of other crystal structures (Ardeljan et al., 2014, 2016a; Ardeljan and Knezevic, 2018; Beyerlein and Tomé, 2008; Feather et al., 2019; Knezevic et al., 2012, 2013, 2016a). In particular, this DD law has been applied previously for the two materials used here: Mg–4Li and pure Nb (Knezevic et al., 2014c; Risse et al., 2017; Zecevic et al., 2018a). Prior studies involving an integration of experimental testing, texture evolution, and polycrystal modeling with the DD model have suggested that the Mg–4Li generally deforms by a combination of the basal, prismatic, and pyramidal type I and II $< \mathbf{c}+\mathbf{a} >$ slip families in tension, compression, and rolling (Risse et al., 2017; Zecevic et al., 2018a). The same analyses indicate that glide on {110} and {112} slip systems can reproduce the yield surfaces, stress-strain response, and texture evolution. In the light of these works, we used the DD model parameters in the EPSC calculations presented in Tables 4 and 5. In appendix A, we provide a review of the DD model formulation, and Tables 4 and 5 present the DD model parameters for the Mg–4Li and Nb phases, respectively. In the case of Mg–4Li, we adopt the best fit case of (Zecevic et al., 2018a), noting that q^{α} which governs the debris dislocation generation and hardening at large strains, is purposely set to zero, resulting in perfect plasticity after strains of approximately 30%. In prior modeling cases, the mechanical behavior of Mg–4Li was reproduced for low strains and at larger grain sizes. Reductions in grain size have been reported in (Risse et al., 2017) to result in a higher CRSS for prismatic $< \mathbf{a} >$ slip. Thus, it is reasonable to expect that some small changes to the material parameters would be needed. In the absence of large stress strain data, we take a modified approach to that presented in (Agnew et al., 2001) and set $q^{\alpha} = 0$ so that no debris dislocation generation occurs and no hardening occurs after approximately 30% plane-strain-deformation. Therefore, a change in the CRSS will change the ratio of slip resistances at larger strains.

4.4. Mg–4Li/Nb model input and set up

For the ARB material reported here, we applied EPSC to each phase in order to determine the deformation mechanisms responsible for texture evolution. The calculations consider the single phase of either Mg–4Li or Nb, deforming alone and not together as a composite. The choice to leave the phases uncoupled stems from i) the experimental observation that both phases accommodated similar levels of strain and ii) from the findings of past crystal plasticity finite element modeling of Zr/Nb, which revealed that coupling of layers at the present length scale of 200 μm is not relevant to capturing the deformation behavior (Ardeljan et al., 2014).Because Nb microstructure and dislocation density did not appear affected by the annealing steps, a single simulation is performed from the annealed initial microstructure presented in Fig. 6, whereas for the Mg–4Li the annealed texture from the previous rolling or ARB step, shown in Fig. 6, was used to initialize the model. For both phases, 5000 equally weighted grains are used to create the representative model polycrystal. Rolling is simulated by applying plane strain compression with a strain-rate of $5s^{-1}$.

Table 4
DD parameters for the Mg–4Li phase as fitted in (Risse et al., 2017) to stress strain and later modified to account pyramidal features in rolled texture in (Zecevic et al., 2018a).

		< a > prism	< a > basal	< c+a > pyr I	< c+a > pyr II
$\tau_{0,f}^{\alpha}$ [MPa]	A^{α}	2.39×10	1.16	1.21×10^{2}	1.38×10^{2}
	B^{α}	3.84×10^{-2}	2.09×10^{-2}	2.15×10^{-2}	2.15×10^{-2}
	C^{α}	4.27×10^{2}	3.81×10^{2}	3.57×10^{2}	3.57×10^{2}
k_{I}^{α} [m^{-1}]		8×10^{8}	8×10^{7}	7.5×10^{7}	7.5×10^{7}
D^{α} [MPa]	E^{α}	3.2×10^{3}	1.5×10^{3}	3.3×10^{3}	3.3×10^{3}
	F^{α}	2.18×10^{9}	0.0	0.0	0.0
	G^{α}	-3.68×10^{-2}	1.0	1.0	1.0
g^{α}	–	3.3×10^{-3}	2.0×10^{-3}	2.0×10^{-3}	2.0×10^{-3}
$\dot{\varepsilon}_0$ [s^{-1}]		10^{7}	10^{7}	10^{7}	10^{7}
ρ_0 [m^{-2}]		1.5×10^{12}	1.5×10^{12}	1.5×10^{12}	1.5×10^{12}
χ		0.9	0.9	0.9	0.9
q^{α}		0	0	0	0
$\beta = 1$	TTW				
FIF (finite initial fraction)	0.015				
τ_0^{β} (MPa)	25.0				
Latent hardening from slip to TTW ($C^{\alpha\beta}$)		50	50	450	450

Table 5
DD parameters for the Nb phase taken, with the exception of $\tau_{o,f}^{\alpha}$, from (Knezevic et al., 2014c).

α – Slip mode	{110} & {112} *Slip*
$\tau_{o,f}^{\alpha}$ [MPa]	102 & 92
k_{I}^{α} [m^{-1}]	0.5×10^{8}
g^{α}	3.2×10^{-2}
D^{α} [MPa]	70
$\dot{\varepsilon}_0$ [s^{-1}]	10^{7}
q^{α}	14

We utilize for Mg–4Li the experimentally reported ellipsoid ratios for 2.5 : 1 RD: ND and 1 : 1: 1 RD: TD: ND for Nb. The ellipsoidal shapes for all grains are allowed to evolve as a mean ellipsoid shape.

5. Modeling results and analysis of deformation mechanisms

Fig. 12 through 15 show simulations of texture evolution of the Mg–4Li phase with the aim of revealing the effect of grain shape and fragmentation, as well as the effective medium coupling with activation of pyramidal slip. In Fig. 12 through 14, basal and prismatic pole figures are presented for both the model and experiment. The corresponding relative activities of the three HCP slipmodes—basal < **a** > , prismatic < **a** > , and pyramidal < **c**+**a** > type I and II, as well as the tensile twinning—are provided as a function of applied straining. The relative activities are defined by the sum of shear increments for each slip system divided by the sum of all shear increments over all of the slip systems. In Fig. 15, we show the variation in M^{eff}, which is calculated as the volume average over polycrystal at each strain increment.

Figs. 12 and 13 show the calculated texture of the Mg–4Li phase using the parameters in Table 4. For comparison with the ARB simulations, the results of (Zecevic et al., 2018a) are shown in Fig. 12a, wherein a plane strain compression simulation with a 54% reduction is performed with the hot extruded sheet texture, shown in Fig. 9, as the starting texture. The deformed experiment texture is reproduced with similar contributions of basal, prismatic, and pyramidal I with a small amount of pyramidal II and twinning. As noted in (Tomé, 1999), prismatic slip does not reorient the **c**-axis in RD, but the **c**-axis is controlled by the pyramidal slip activity and to a lesser extent the rigid rotation of the ellipsoid grain—a result of the HEM formulization. Thus, the **c**-axis collapse to ND in the third ARB cycle is likely due to a decrease in pyramidal activity which could be driven by a change in the HEM or change in slip resistances. Fig. 12 straight-rolled simulation was produced with M^{eff} of 1, which is the secant approach to defining grain interaction strength. We found when adjusting CRSS ratios to capture the peak collapse of the third ARB cycle, that with the secant approach and the starting texture of ARB 2 AN, it was not possible to limit pyramidal activity to the point that peak collapse would happen. This is not surprising since the secant approach is known to stabilize higher levels of prismatic slip than tangent or RDC approaches (Tomé, 1999). Notwithstanding that grain size may affect slip resistances, the motivation for the simulations in Figs. 12 and 13 is to determine whether the expected reduction in pyramidal activity is captured by the model with the experimental starting textures and

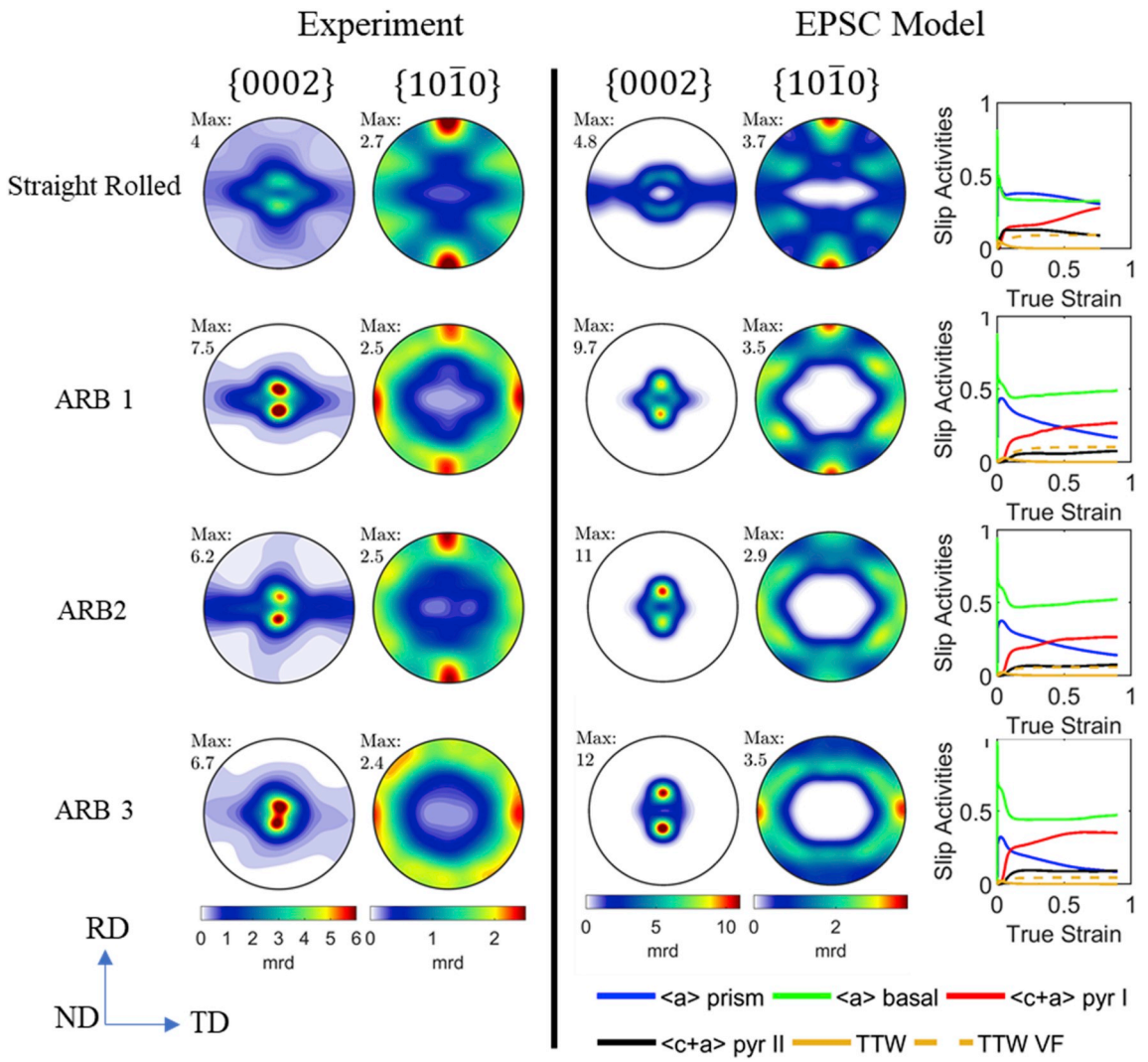

Fig. 12. Experimental and model textures using the parameters presented in Table 4. The 54% straight rolled simulation case from (Zecevic et al., 2018a) is initialized from the hot extruded texture shown in Fig. 9, and each ARB simulation is initialized with the texture from the annealed prior case. Model pole figures are reported at the same strain level as the experimental pole figures.

the RDC defined HEM.

The EPSC simulations of the ARB process are presented in Fig. 12. The effects on slip activities due to the evolving texture over the ARB process are i) decreasing amounts of prismatic slip, ii) increasing amounts of pyramidal slip, and iii) decreasing amounts of twinning. We also observe for ARB 1 and ARB 2 that the stabilization of the prismatic plane parallel to RD requires significant prismatic slip, and the transition toward the prismatic plane aligned with TD is driven by pyramidal slip. Notably, the textures for ARB 1 and ARB 2 are captured satisfactorily, and evolution pyramidal I and prismatic slip have the desired effect on the prismatic pole figure. The discrepancy, however, is that the **c**-axis peak collapse of ARB 3 is not captured. This difference suggests that, at least for ARB 3, the amount of pyramidal slip is not being predicted appropriately by the model. The M^{eff} evolution with strain is presented in Fig. 15 for the ARB simulations in Fig. 12, revealing that the effective mediums for ARB 1 and ARB 2 are between 0.7 and 0.8, while for ARB 3, M^{eff} lies between 0.8 and 0.9, reinforcing that the increase in pyramidal activity is highly coupled to texture and the HEM. Since the basal pole figure does not evolve substantially between ARB 1 AN and ARB 2 AN texture, we infer the transition of $\{10\bar{1}0\}$ planes aligned with RD toward TD result in an increased M^{eff} for the model parameter in Table 4.

To explore the effect of grain shape and fragmentation, which are expected to have some effect on the HEM (Tomé, 1999) and on the evolution of texture, three additional cases are simulated for the ARB 3 case. An ellipsoid grain aspect ratio (GAR) of 2.5 : 1: 1 (RD: TD: ND) was used in Fig. 12 ARB 3. The additional cases of GAR 2.5 : 1.5: 1 and 2.5 : 2.5: 1 are also simulated and shown in Fig. 13. These cases together explore the contribution of grain aspect ratio on HEM stiffness. An extreme case of fragmentation is also simulated by not allowing the ellipsoid shape to evolve and setting the ellipsoid grain aspect ratio to 1:1:1. The simulations exploring the size of TD relative RD and ND in Fig. 13 reveal that pyramidal I and pyramidal II can be progressively suppressed by increasing

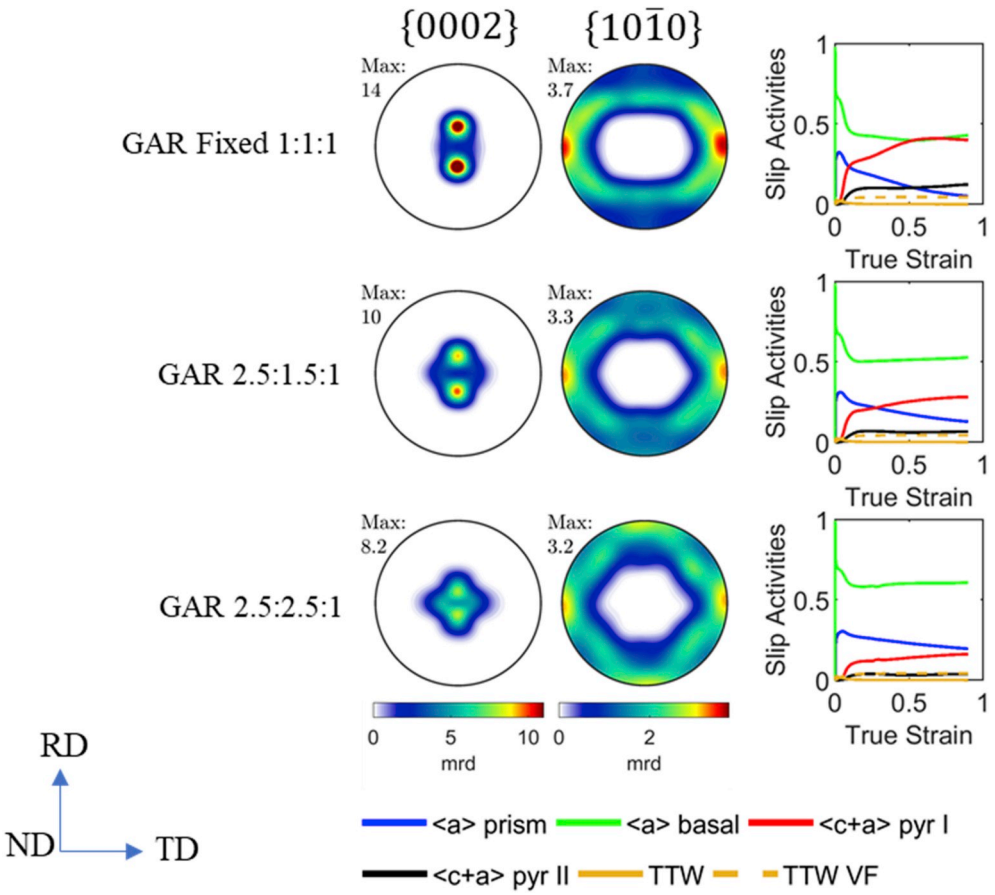

Fig. 13. The effect of grain aspect ratio (GAR)and grain shape evolution on slip activity using the parameters in Table 4.

the relative TD grain size. Fig. 13 shows a commiserate decrease in M^{eff} with decreasing pyramidal activity, as observed in the ARB simulation in Fig. 12. There is no effect in the M^{eff} due to fixing the ellipsoid shape at the GAR 1 : 1: 1 compared to 2.5 : 1: 1; however, there is a small increase in pyramidal I and decrease in basal activity. These results combined suggest that fragmentation limiting rigid rotation out of the ND plane would have significant influence on the effective medium and reduce the activity of pyramidal slip.

Comparing the case of GAR 2.5 : 2.5: 1 in Fig. 13 to 2.5 : 1.5: 1 in Fig. 13, we observe larger TD to ND ratios stabilize the prismatic plane along RD; therefore, it is not likely that the grain shape alone will result in basal peak collapse towards ND while the prismatic planes align with TD.

To see the effect of an increase in basal activity on texture evolution, we repeated the calculations using higher pyramidal I and II initial slip resistances (raised to 138 and 150 respectively) and the results are shown in Fig. 14. We find that increases in these two resistances lead to a substantial increase in the flow stress and a reduction in pyramidal slip activities that collapse the basal poles towards ND. We also explore in Fig. 14 the effect of elevating prismatic slip, since this slip mode is reported to be affected by grain size in (Lentz et al., 2015). We find that with a large increase in prismatic slip resistance, the effect on texture evolution is to lower the intensity of the maxima. Yet the change in slip resistance is not enough to affect the location of the texture maxima. Finally, a combination of raised prismatic and pyramidal slip that results in a similar peak split as in the raised pyramidal case is presented in Fig. 14. Taken together, we find that the peak split arises from the slip resistance ratios used in these cases, and on this basis we conclude that the relative slip parameters are not unique when only provided the texture and the model utilizing the RDC method.

One of the main predictions of the model is the set of slip strengths that underlie the observed texture evolution. Fig. 14 shows the corresponding relative activities of the three HCP slip modes: basal $< \mathbf{a} >$, prismatic $< \mathbf{a} >$, and pyramidal $< \mathbf{c}+\mathbf{a} >$ type I and II, as a function of applied straining for the final ARB pass. As shown, basal and prismatic slip are the dominant slip contribution to the deformation during rolling pass, whereas pyramidal $< \mathbf{c}+\mathbf{a} >$ type I has increasing contribution at the expense of prismatic slip, while pyramidal $< \mathbf{c}+\mathbf{a} >$ type II has a constant, small contribution to accommodating plastic deformation. More pyramidal I results in peak split towards RD as reported in (Tomé, 1999). Pyramidal II stabilizes the prismatic plane aligned with RD but also contributes to the reorientation of orientations toward TD as reported in (Zecevic et al., 2018a). The absolute intensities of the pole figures are likely influenced by continuous dynamic recrystallization mechanisms. The inclusion of misorientation spreads based on second moments of stress and spin can reduce the intensity of the deformed texture and thus improve the texture predictions (Lebensohn et al., 2016; Zecevic et al., 2018b, 2019). Accounting for intra-granular misorientation is a direction of future modeling (Zecevic

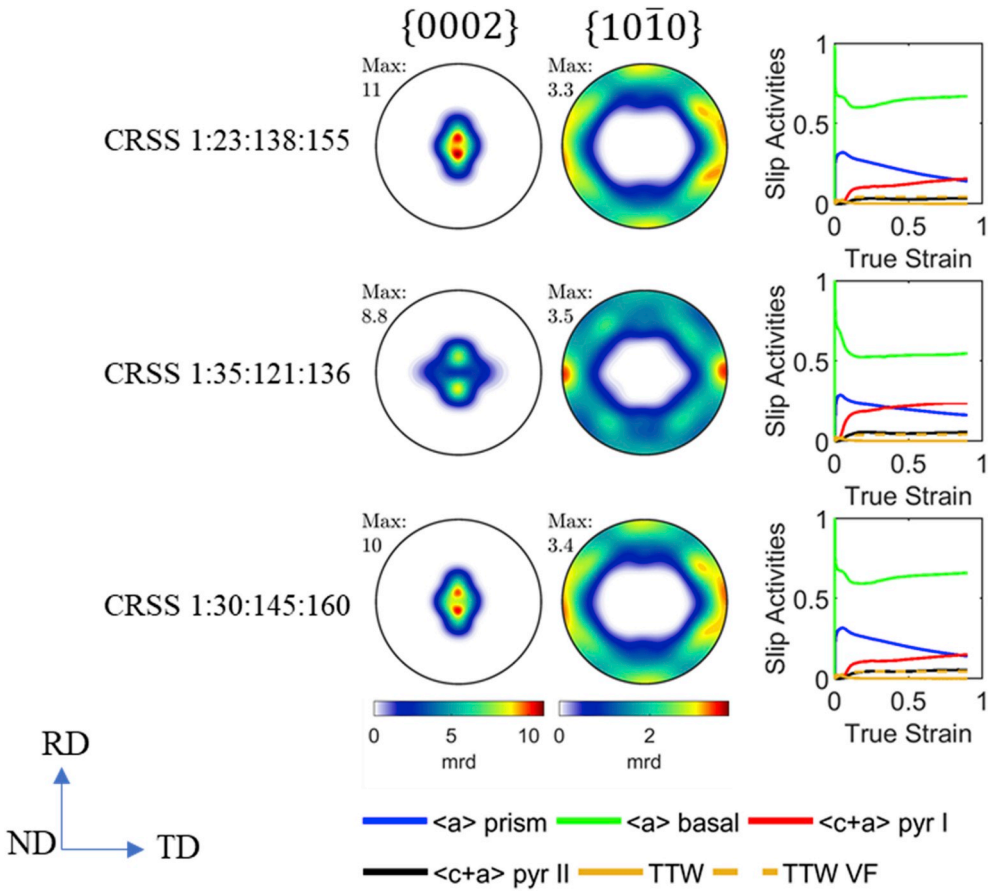

Fig. 14. Using a grain aspect ratio of 2.5 : 1.5: 1, the initial CRSS are adjusted from those reported in Table 4 to suppress pyramidal I and II, to suppress prismatic slip, and to suppress both prismatic pyramidal affecting different ratios of prismatic to pyramidal slip resistance. The values were adjusted to achieve similar texture features as observed experimentally.

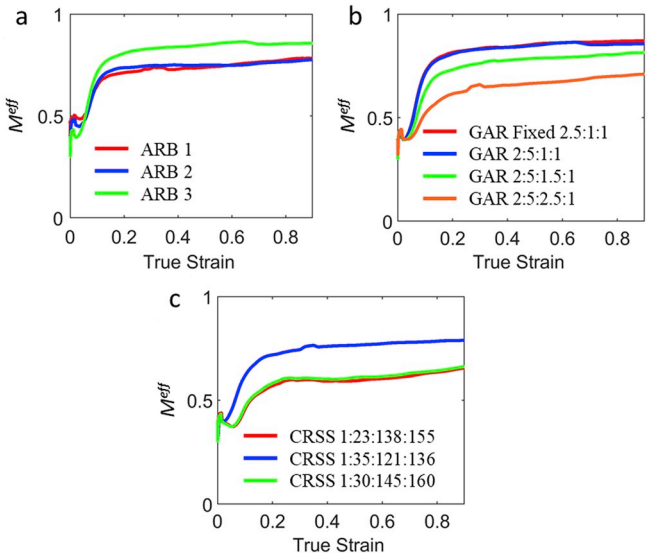

Fig. 15. Evolution of M^{eff} for Mg–4Li cases presented in (a) Fig. 12, (b) Fig. 13, and (c) Fig. 14.

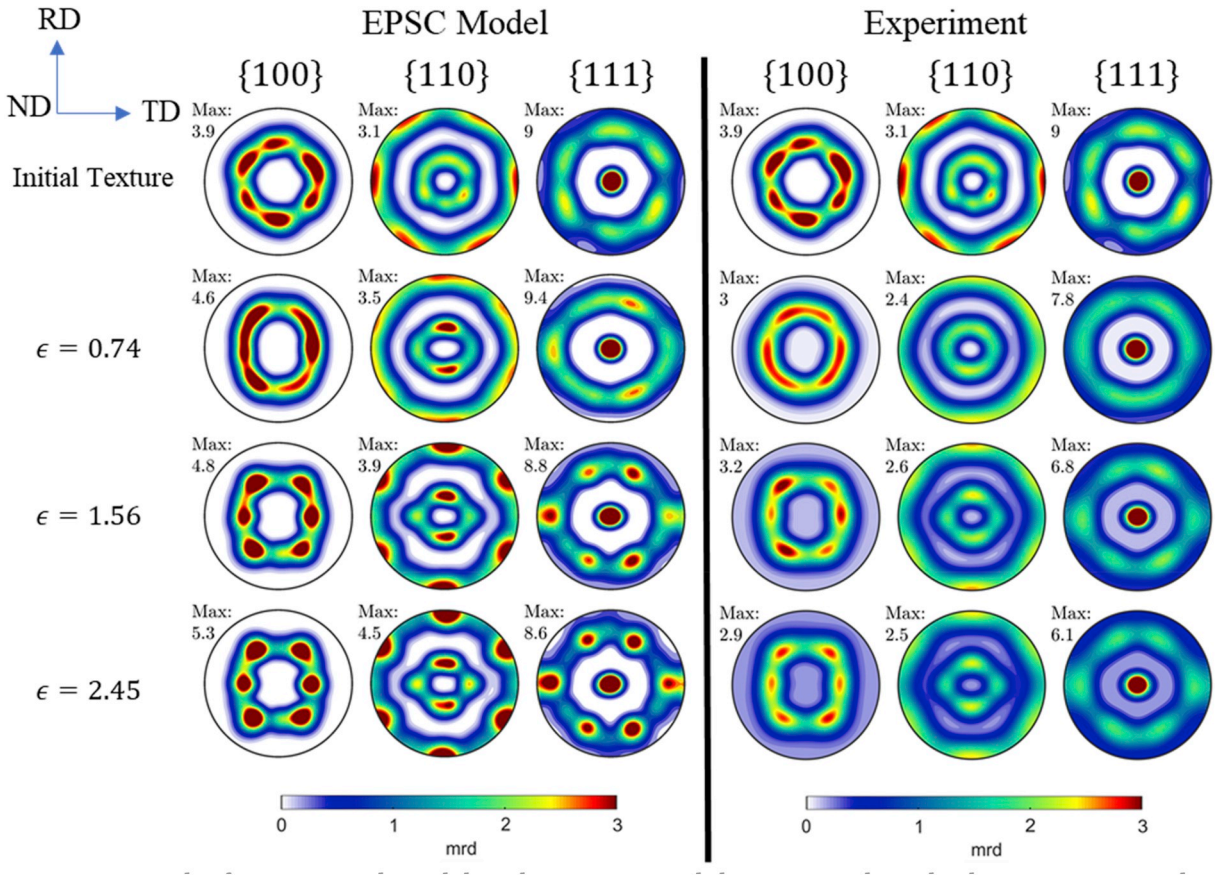

Fig. 16. Pole figures predicted by the EPSC model compared with the experimental texture from Neutron diffraction and EBSD.

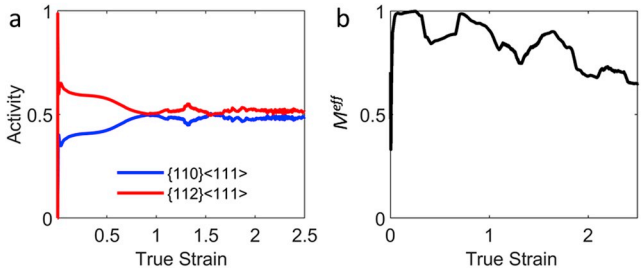

Fig. 17. The slip activities predicted by EPSC for Nb (a) and the corresponding evolution of the M^{eff} predict using RDC (b).

et al., 2017b, 2019).

Fig. 16 compares the modeling predictions to the experimental pole figures, and Fig. 17a shows the corresponding slip mode activities in the Nb phase as predicted by EPSC. Typically, the two slip families are considered and enforced to have equal strengths. Here we find that the best agreement is achieved when the slip strength for {112} slip is approximately 10% easier than that for {110} slip (see Table 5 for parameters). Previous lower length scale calculations support this finding. Atomistic calculations of core structures and motion of {112} dislocations of screw character show that it responds to non-Schmid stresses and are dependent on whether they were acting in the twinning or non-twinning sense (Ito and Vitek, 2001). In earlier discrete dislocation dynamics simulations, the asymmetric non-Schmid effect was incorporated into the Peierls barrier term for {112} glide, in addition to the non-Schmid effect characteristic of {110} glide (Wang and Beyerlein, 2011). Taken together, the {112} glide in the twinning sense was comparatively easier than {110} glide, which were easier than {112} glide in the anti-twinning sense. Deformation simulations of single BCC crystals showed that incorporating asymmetric {112} non-Schmid effects was necessary for capturing the tension-compression asymmetry seen experimentally (Savage et al., 2017, 2018).

Nb is well known for its tendency to develop shear bands, causing a more distributed and diffuse γ-fibre, which in turn would reduce the texture intensity, as shown in Fig. 10 and in the EBSD of Nb in Fig. 6. Consequently, reorientation rates to stable texture

components are faster in the calculation than actuality, leading to the development of stronger textures than measured. Unlike the evolution in M^{eff} for Mg–4Li shown in Fig. 15, the M^{eff} in Fig. 17b fluctuates often and exhibits a trend toward a polycrystal with harder grains. Indeed, this is likely due to the very sharp texture and highly elongated grains, as is the slight oscillations in slip activity shown in Fig. 14c.

Besides the excellent agreement with experimental texture components, the RDC approach enabled use of the annealed Nb texture. In previous works, such as (Knezevic et al., 2014c) a random texture was used to initialize the models because it was not possible to break the stable gamma fiber and get satisfactory results with a single effective medium scheme.

6. Discussion

Critical to the success of processing Mg-xLi/Nb laminates was achieving co-deformation between the two phases over a relatively large straining period (> 50% strain). HCP metals, such as Mg, are typically highly plastically anisotropic, especially compared to BCC materials like Nb. Large differences in deformation response between the two phases and the onset of localization in the HCP phase have typically thwarted laminate processing in nearly all prior attempts to deform Mg-based laminates to extreme strains. Here, microscopy, diffraction, hardness measurements, and analysis of deformation mechanisms via multiscale modeling were employed to understand the underlying processes facilitating co-deformation. First, the microstructural characterization has revealed that the Mg–4Li alloy exhibited minimal twinning after ARB cycles and that the variation in **c**-axis peak position in the highest reduction specimen is accompanied by dynamic recrystallization. While the former can reduce, the latter can increase local heterogeneities. Additionally, the Nb phase showed some local geometric softening effects that could lead to interface waviness and shear band formation. Restoring these effects in the Nb phase requires annealing at a much higher temperature than 200 °C. Nevertheless, the evolution of the overall strength differential between co-deforming phases with strain is characterized to be low enough to facilitate bonding without instabilities. Here, the hardness evolution of the Mg alloy and Nb phases after rolling and annealing was measured and used as the indication of strength. The hardness of the Mg phase did not change appreciably from pass to pass, a result of the intermediate annealing which effectively resets the microstructure. While the Nb phase had very little work hardening, the Mg alloy phase had significant work hardening and consequently, the difference in strength between the two phases increase with strain during each ARB pass.

The mismatch in the coefficient of linear thermal expansion (CLTE) and the shear modulus assuming a randomly texture polycrystal is Mg: Nb 4.0 (Kúdela et al., 2007) (Chen and Boyle, 2009; Wang and Reeber, 1998) and 0.42 (Bolef, 1961; Tromans, 2011) respectively. The mismatch is substantial compared to previous ARB HCP/X material systems reported in literature. The CLTE mismatch is known, for thicker microlaminates on the order of 700μm, to create shear stresses at the interfaces during cooling that promote delamination (Lesuer et al., 1996). Since i) the laminates were bonded enough to allow the removal of edge cracks, ii) the ARB process was successfully applied, and iii) the shear stress diminishes with layer refinement, the CLTE mismatch does not appear to be a limiting factor in processing Mg/Nb to nanolaminates. However, the CLTE mismatch may create residual stresses or potentially microstructural artifacts such as the tensile twins in Fig. 5 depending on the constraint posed by Mg/Nb interface (Lesuer et al., 1996). Similar to the CLTE, the elastic modulus mismatch is known to have some influence on toughness and promote crack initiation in the ductile phase (Lesuer et al., 1996).

The elastic modulus mismatch may also play a role in co-deformation during rolling. The layered structure achieved in Fig. 3 and the analysis of the average layer thickness in Table 2 suggest that Mg–4Li and Nb stretch and thin at the same rate, though the Nb phase has a less homogenous layer morphology. For a given plane strain compression level, the phases must have different stresses. However, the role of modulus mismatch on stress transfer between the phases (Pu and Gao, 2015) and strain partitioning between deformation modes is not clear, especially considering that complex deformation processes can cause Nb to thin. Using finite element analysis of rolling multilayers (Govindaraj et al., 2013) reported that the bending and unbending caused by a shear front during the rolling processes can uniformly reduce the stronger phase as long as there is work hardening. Once there is no working hardening, layer pinch off is likely to occur. While there have been studies that explore the contribution to hardening rate, strength differential, and localization mechanisms (Govindaraj et al., 2013; Yazar et al., 2005), there has not been an effort to systematically explore elastic parameter mismatch or the stability condition for only one phase work hardening as is seen in this Mg-xLi/Nb composite.

An interesting result arises from the polycrystal calculations of the slip mechanisms. In the calculations of texture evolution in the Mg–4Li phase, four slip modes and a tensile twinning mode were made available to model the polycrystals. The rolling simulations that properly replicated the neutron diffraction texture measurements after each pass indicated that only a small amount of extension twinning was active (in agreement with the EBSD measurements) and the activity of pyramidal < **c** + **a** > slip is less in ARB 3 compared to rolling from the Mg–4Li hot extruded sheet. The model results show at low strain that plastic deformation in rolling is accommodated primarily by easier-to-activate < **a** > slip modes: prismatic < **a** > and basal < **a** > slip. At larger strains there is an increasing, but minimal contribution from pyramidal slip. Predominance of the easy slip systems over the harder one and over twinning, which can cause localized, subcrystalline scale shearing, likely contributed to the formability of the Mg phase during the ARB processing.

It is worth remarking on the paucity of deformation twinning, since Mg alloys are generally expected to be prone to deformation twinning. In this particular study, the orientation relationship between the initial texture and applied deformation state of plane strain compression are not conducive for extensive {1012} extension twinning. The initial texture and rolling deformation are, however, oriented well for contraction twinning. In prior work, profuse {1011} contraction twinning and {1011}-{1012} double twinning of this Mg–4Li alloy have been reported with average grain sizes of 23 μm, but not in a material with average grain sizes of 5 μm. In the material studied here, the average grain size was approximately 9 μm at the beginning of the second and third passes, and

the finest size of the grains after these passes was on average 2 μm through the thickness. Most of the twinning developed in the first pass, but the volume fraction did not increase with the number of passes. Furthermore, in the second and third passes the material underwent dynamic recrystallization. The refinement of grain sizes via deformation and recrystallization would explain the low occurrence twinning in this material.

7. Conclusions

In this work, we employed the ARB process to manufacture Mg alloy/Nb laminates for the first time with an average 200 μm individual layer thickness for both phases. One of two types of Mg-xLi alloys was roll bonded with high-purity Nb: either an Mg–4Li alloy or an Mg–5Li alloy (wt. %). The following conclusions are drawn:

- The deformation twinning type and fractions, grain size and shape, and texture evolution were assessed via EBSD and neutron diffraction, and with these measurements no appreciable differences were observed between Mg–4Li and Mg–5Li, despite the two alloys starting with different textures.
- To achieve the fine layer thickness, three ARB sequences were used and static annealing of 200 °C for 1 h were applied after ARB passes. Up to three passes, the layers remained continuous and polycrystalline even though the strength different between Nb and Mg was as high as 3.75. However, edge cracking prevented further processing. For future attempts to succeed in reaching the nano structuring, edge cracking must be limited.
- Annealing altered the texture of the Mg alloy and reset the grain shape to equiaxed and grain size to ~9 μm, but it did not alter the microstructure of Nb. The deformation of Nb was slightly more inhomogeneous, which is manifested with more variation in the Nb layer thickness than in the Mg layer thickness.
- To determine the possible slip modes involved, we applied a polycrystal model, EPSC, and used the RDC scheme to account for possible directional anisotropy in the interactions between the grains within the individual phases. The RDC values were different between the Mg and Nb phases, which reflect the fact that they do not have similar anisotropies: Nb phase is not nearly as plastically anisotropic as the Mg alloy phase. Although the RDC scheme is not new, it is not common to apply it in conventional single-phase materials. Yet considering the dissimilarity in deformation of the two-phase system of interest here, and the coupling between slip resistances and the HEM, we found it to be essential in capturing texture evolution.

Acknowledgments

The authors gratefully acknowledge support from the U.S. National Science Foundation (NSF) under grant No. CMMI-1727495 (UNH) and CMMI-1728224 (UCSB). D.J.S. also acknowledges an NSF Graduate Research Fellowship. This work was performed, in part, at the Center for Integrated Nanotechnologies, an Office of Science User Facility operated for the U.S. Department of Energy (DOE) Office of Science. The authors acknowledge discussions about ARB processing and material characterization with Nan Li and John S. Carpenter.

Appendix B. Supplementary data

Supplementary data to this article can be found online at https://doi.org/10.1016/j.ijplas.2019.08.015.

Appendix A

Here, we show a summary of a dislocation density hardening law formulation used to compute the evolution of slip and twin resistances as a function of strain, temperature and strain rate (Risse et al., 2017; Zecevic et al., 2018a). An assumption is made that all slip and twin systems within the same deformation mode share the same values for critical resolved shear stress (CRSS).

The critical resolved shear stress for activation of slip considers contributions of several different terms: a friction stress $\tau_{0,f}^{\alpha}$, a forest dislocation interaction stress τ_{for}^{α} and a dislocation substructure interaction stress τ_{sub}^{α}:

$$\tau_c^{\alpha} = \tau_{0,f}^{\alpha} + \tau_{for}^{\alpha} + \tau_{sub}^{\alpha}, \quad \tau_{0,f}^{\alpha} = \frac{A^{\alpha}}{1 + \exp(B^{\alpha}(T - C^{\alpha}))} \tag{A1}$$

The model for the critical resolved shear stress for twin activation differs from that for slip. It accounts two distinct contributions: a temperature-independent friction term τ_0^{β} and a latent hardening term coupling the active slip and the twin systems. Taken together, the critical resolved shear stress for twinning can be expressed as:

$$\tau_c^{\beta} = \tau_0^{\beta} + \mu^{\beta} \sum_{\alpha} C^{\alpha\beta} b^{\beta} b^{\alpha} \rho_{for}^{\alpha} \tag{A2}$$

Here μ^{β}, b^{β} and $C^{\alpha\beta}$ represent the elastic shear modulus, Burgers vector on the given twin system, and the latent hardening matrix used for coupling, respectively. The behavior of τ_{for}^{α} and τ_{sub}^{α} is governed by the evolution of the dislocation densities in the form of forest ρ_{for}^{α} and substructure ρ_{sub}^{α} dislocations. These relationships, for each dislocation type, can be expressed in the form of a Taylor law:

$$\tau_{for}^{\alpha} = \chi b^{\alpha}\mu^{\alpha}\sqrt{\rho_{for}^{\alpha}},\ \ and\ \tau_{sub}^{\alpha} = k_{sub}\mu^{\alpha}b^{\alpha}\sqrt{\rho_{sub}}log\left(\frac{1}{b^{\alpha}\sqrt{\rho_{sub}}}\right) \tag{A3}$$

where $\chi = 0.9$ is a dislocation interaction parameter, μ^{α} is the shear modulus and $k_{sub} = 0.086$ is a mathematical parameter that insures that Eq. (A3) compensates the Taylor law at low dislocation densities. The stored forest density ρ_{for}^{α} evolves via a competition between the rate of storage and the rate of dynamic recovery:

$$\begin{aligned}&\frac{\partial\rho_{for}^{\alpha}}{\partial\gamma^{\alpha}} = \frac{\partial\rho_{gen,for}^{\alpha}}{\partial\gamma^{\alpha}} - \frac{\partial\rho_{rem,for}^{\alpha}}{\partial\gamma^{\alpha}} = k_1^{\alpha}\sqrt{\rho_{for}^{\alpha}} - k_2^{\alpha}(\dot{\varepsilon},\mathrm{T})\rho_{for}^{\alpha},\\ &\Delta\rho_{for}^{\alpha} = \frac{\partial\rho_{for}^{\alpha}}{\partial\gamma^{\alpha}}|\Delta\gamma^{\alpha}|\end{aligned} \tag{A4}$$

where k_1^{α} is a coefficient for the rate of dislocation storage due to statistical trapping of gliding dislocations by the forest obstacles and k_2^{α} is the coefficient for the rate of dynamic recovery, which is given by the following expression:

$$\frac{k_2^{\alpha}(\dot{\varepsilon},\mathrm{T})}{k_1^{\alpha}} = \frac{\chi b^{\alpha}}{g^{\alpha}}\left(1 - \frac{kT}{D^{\alpha}b^3}ln\left(\frac{\dot{\varepsilon}}{\dot{\varepsilon}_0}\right)\right),\ D^{\alpha} = E^{\alpha} + F^{\alpha}\exp G^{\alpha}T \tag{A5}$$

In Eq. (A5), k, $\dot{\varepsilon}_0$, g^{α} and D^{α} are respectively Boltzmann's constant, a reference strain rate, an effective activation enthalpy and a drag stress. Furthermore, the increment in substructure development is proportional to the rate of dynamic recovery of all active dislocations and can be expressed as:

$$\Delta\rho_{sub} = \sum_{\alpha} q^{\alpha}b^{\alpha}\frac{\partial\rho_{rem,for}^{\alpha}}{\partial\gamma^{\alpha}}|\Delta\gamma^{\alpha}| \tag{A6}$$

where q^{α} is a coefficient defining the fraction of an α-type dislocations that do not annihilate but become substructure dislocation. The hardening parameters have been calibrated in the earlier study and used here.

References

Agnew, S.R., Yoo, M.H., Tomé, C.N., 2001. Application of texture simulation to understanding mechanical behavior of Mg and solid solution alloys containing Li or Y. Acta Mater. 49, 4277–4289.

Agnew, S.R., Senn, W., J.Horton, J., 2006. Mg Sheet Metal Forming: Lessons Learned from Deep Drawing Li and Y Solid-Solution Alloys.

Al-Samman, T., Gottstein, G., 2008. Dynamic recrystallization during high temperature deformation of magnesium. Mater. Sci. Eng. A 490, 411–420.

Ardeljan, M., Knezevic, M., 2018. Explicit modeling of double twinning in AZ31 using crystal plasticity finite elements for predicting the mechanical fields for twin variant selection and fracture analyses. Acta Mater. 157, 339–354.

Ardeljan, M., Beyerlein, I.J., Knezevic, M., 2014. A dislocation density based crystal plasticity finite element model: application to a two-phase polycrystalline HCP/BCC composites. J. Mech. Phys. Solids 66, 16–31.

Ardeljan, M., Knezevic, M., Nizolek, T., Beyerlein, I.J., Mara, N.A., Pollock, T.M., 2015. A study of microstructure-driven strain localizations in two-phase polycrystalline HCP/BCC composites using a multi-scale model. Int. J. Plast. 74, 35–57.

Ardeljan, M., Beyerlein, I.J., McWilliams, B.A., Knezevic, M., 2016a. Strain rate and temperature sensitive multi-level crystal plasticity model for large plastic deformation behavior: application to AZ31 magnesium alloy. Int. J. Plast. 83, 90–109.

Ardeljan, M., Savage, D.J., Kumar, A., Beyerlein, I.J., Knezevic, M., 2016b. The plasticity of highly oriented nano-layered Zr/Nb composites. Acta. Mater. 115, 189–203.

Ardeljan, M., Knezevic, M., Jain, M., Pathak, S., Kumar, A., Li, N., Mara, N.A., Baldwin, J.K., Beyerlein, I.J., 2018. Room temperature deformation mechanisms of Mg/Nb nanolayered composites. J. Mater. Res. 33, 1311–1332.

Barrett, T.J., Knezevic, M., 2019. Deep drawing simulations using the finite element method embedding a multi-level crystal plasticity constitutive law: experimental verification and sensitivity analysis. Comput. Methods Appl. Mech. Eng. 354, 245–270.

Barrett, C.D., Imandoust, A., Oppedal, A.L., Inal, K., Tschopp, M.A., El Kadiri, H., 2017. Effect of grain boundaries on texture formation during dynamic recrystallization of magnesium alloys. Acta Mater. 128, 270–283.

Barrett, T.J., Eghtesad, A., McCabe, R.J., Clausen, B., Brown, D.W., Vogel, S.C., Knezevic, M., 2019. A generalized spherical harmonics-based procedure for the interpolation of partial datasets of orientation distributions to enable crystal mechanics-based simulations. Materialia 6, 100328.

Bay, N., 1983. Mechanisms producing metallic bonds in cold welding. WELDING J 62, 137.

Bay, N., 1986. Cold Welding. Part 2: Process Variants and Applications.

Beyerlein, I.J., Tomé, C.N., 2008. A dislocation-based constitutive law for pure Zr including temperature effects. Int. J. Plast. 24, 867–895.

Bhattacharyya, A., Knezevic, M., Abouaf, M., 2015. Characterization of crystallographic texture and intra-grain morphology in cross-rolled tantalum. Metall. Mater. Trans. A 46, 1085–1096.

Bolef, D.I., 1961. Elastic constants of single crystals of the bcc transition elements V, Nb, and Ta. J. Appl. Phys. 32, 100–105.

Carpenter, J.S., Vogel, S.C., LeDonne, J.E., Hammon, D.L., Beyerlein, I.J., Mara, N.A., 2012. Bulk texture evolution of Cu-Nb nanolamellar composites during accumulative roll bonding. Acta Mater. 60, 1576–1586.

Carpenter, J.S., McCabe, R.J., Zheng, S.J., Wynn, T.A., Mara, N.A., Beyerlein, I.J., 2014. Processing parameter influence on texture and microstructural evolution in Cu-Nb multilayer composites fabricated via accumulative roll bonding. Metall. Mater. Trans. A 45, 2192–2208.

Carpenter, J.S., Nizolek, T., McCabe, R.J., Knezevic, M., Zheng, S.J., Eftink, B.P., Scott, J.E., Vogel, S.C., Pollock, T.M., Mara, N.A., Beyerlein, I.J., 2015a. Bulk texture evolution of nanolamellar Zr–Nb composites processed via accumulative roll bonding. Acta Mater. 92, 97–108.

Carpenter, J.S., Nizolek, T.J., McCabe, R.J., Zheng, S.J., Scott, J.E., Vogel, S.C., Mara, N.A., Pollock, T.M., Beyerlein, I.J., 2015b. The suppression of instabilities via biphase interfaces during bulk fabrication of nanograined Zr. Mater. Res. Lett. 3, 50–57.

Cave, J., 1973. The mechanism of cold pressure welding by rolling. J. Inst. Met. 101, 203–207.

Chang, H., Zheng, M.Y., Xu, C., Fan, G.D., Brokmeier, H.G., Wu, K., 2012. Microstructure and mechanical properties of the Mg/Al multilayer fabricated by accumulative roll bonding (ARB) at ambient temperature. Mater. Sci. Eng. A 543, 249–256.

Chen, K., Boyle, K.P., 2009. Elastic properties, thermal expansion coefficients, and electronic structures of Mg and Mg-based alloys. Metall. Mater. Trans. A 40, 2751.

de Boer, F.R., Boom, R., Miedema, A.R., 1980. Enthalpies of formation of liquid and solid binary alloys based on 3d metals: I. Alloys of scandium, titanium and vanadium. Phys. B+C 101, 294–319.

Dehsorkhi, R.N., Qods, F., Tajally, M., 2011. Investigation on microstructure and mechanical properties of Al–Zn composite during accumulative roll bonding (ARB) process. Mater. Sci. Eng. A 530, 63–72.
Dillamore, I.L., Roberts, J.G., Bush, A.C., 1979. Occurrence of shear bands in heavily rolled cubic metals. Met. Sci. 13, 73–77.
Dinda, G.P., Rösner, H., Wilde, G., 2005. Synthesis of bulk nanostructured Ni, Ti and Zr by repeated cold-rolling. Scr. Mater. 52, 577–582.
Edalati, K., Masuda, T., Arita, M., Furui, M., Sauvage, X., Horita, Z., Valiev, R.Z., 2017. Room-temperature superplasticity in an ultrafine-grained magnesium alloy. Sci. Rep. 7, 2662.
Eshelby, J.D., 1957. The determination of the elastic field of an ellipsoidal inclusion, and related problems. Proc R. Soc. Lond. A 241, 376–396.
Feather, W.G., Ghorbanpour, S., Savage, D.J., Ardeljan, M., Jahedi, M., McWilliams, B.A., Gupta, N., Xiang, C., Vogel, S.C., Knezevic, M., 2019. Mechanical response, twinning, and texture evolution of WE43 magnesium-rare earth alloy as a function of strain rate: experiments and multi-level crystal plasticity modeling. Int. J. Plast. 120, 180–204.
Figueiredo, R.B., Aguilar, M.T.P., Cetlin, P.R., Langdon, T.G., 2014. Processing magnesium alloys by severe plastic deformation. In: IOP Conference Series: Materials Science and Engineering 63, pp. 012171.
Ghalandari, L., Mahdavian, M.M., Reihanian, M., 2014. Microstructure evolution and mechanical properties of Cu/Zn multilayer processed by accumulative roll bonding (ARB). Mater. Sci. Eng. A 593, 145–152.
Ghorbanpour, S., Zecevic, M., Kumar, A., Jahedi, M., Bicknell, J., Jorgensen, L., Beyerlein, I.J., Knezevic, M., 2017. A crystal plasticity model incorporating the effects of precipitates in superalloys: application to tensile, compressive, and cyclic deformation of Inconel 718. Int. J. Plast. 99, 162–185.
Ghorbanpour, S., McWilliams, B.A., Knezevic, M., 2019a. Effect of hot working and aging heat treatments on monotonic, cyclic, and fatigue behavior of WE43 magnesium alloy. Mater. Sci. Eng. A 747, 27–41.
Ghorbanpour, S., McWilliams, B.A., Knezevic, M., 2019b. Low-cycle fatigue behavior of rolled WE43-T5 magnesium alloy. Fatigue Fract. Eng. Mater. Struct. 42, 1357–1372.
Govindaraj, N.V., Frydendahl, J.G., Holmedal, B., 2013. Layer continuity in accumulative roll bonding of dissimilar material combinations. Mater. Des. 52, 905–915 1980-2015.
Ham, B., Zhang, X., 2011. High strength Mg/Nb nanolayer composites. Mater. Sci. Eng. A 528, 2028–2033.
Ito, K., Vitek, V., 2001. Atomistic study of non-Schmid effects in the plastic yielding of bcc metals. Philos. Mag. A 81, 1387–1407.
Jahedi, M., Knezevic, M., Paydar, M., 2015a. High-pressure double torsion as a severe plastic deformation process: experimental procedure and finite element modeling. J. Mater. Eng. Perform. 24, 1471–1482.
Jahedi, M., Paydar, M.H., Knezevic, M., 2015b. Enhanced microstructural homogeneity in metal-matrix composites developed under high-pressure-double-torsion. Mater. Char. 104, 92–100.
Jahedi, M., Ardjmand, E., Knezevic, M., 2017a. Microstructure metrics for quantitative assessment of particle size and dispersion: application to metal-matrix composites. Powder Technol. 311, 226–238.
Jahedi, M., Beyerlein, I.J., Paydar, M.H., Zheng, S., Xiong, T., Knezevic, M., 2017b. Effects of pressure and number of turns on microstructural homogeneity developed in high-pressure double torsion. Metall. Mater. Trans. A 48, 1249–1263.
Jahedi, M., McWilliams, B.A., Moy, P., Knezevic, M., 2017c. Deformation twinning in rolled WE43-T5 rare earth magnesium alloy: influence on strain hardening and texture evolution. Acta Mater. 131, 221–232.
Jahedi, M., McWilliams, B.A., Kellogg, F.R., Beyerlein, I.J., Knezevic, M., 2018a. Rate and temperature dependent deformation behavior of as-cast WE43 magnesium-rare earth alloy manufactured by direct-chill casting. Mater. Sci. Eng. A 712, 50–64.
Jahedi, M., McWilliams, B.A., Knezevic, M., 2018b. Deformation and fracture mechanisms in WE43 magnesium-rare earth alloy fabricated by direct-chill casting and rolling. Mater. Sci. Eng. A 726, 194–207.
Kelly, E.W., Hosford, W.F., 1968. Plane-strain compression of magnesium and magnesium alloy crystals. Trans. Metall. Soc. AIME 242, 5–13.
Knezevic, M., Beyerlein, I.J., 2018. Multiscale modeling of microstructure-property relationships of polycrystalline metals during thermo-mechanical deformation. Adv. Eng. Mater. 20, 1700956.
Knezevic, M., Bhattacharyya, A., 2017. Characterization of microstructure in Nb rods processed by rolling: effect of grooved rolling die geometry on texture uniformity. Int. J. Refract. Metals Hard Mater. 66, 44–51.
Knezevic, M., Kalidindi, S.R., 2007. Fast computation of first-order elastic-plastic closures for polycrystalline cubic-orthorhombic microstructures. Comput. Mater. Sci. 39, 643–648.
Knezevic, M., Landry, N.W., 2015. Procedures for reducing large datasets of crystal orientations using generalized spherical harmonics. Mech. Mater. 88, 73–86.
Knezevic, M., Capolungo, L., Tomé, C.N., Lebensohn, R.A., Alexander, D.J., Mihaila, B., McCabe, R.J., 2012. Anisotropic stress-strain response and microstructure evolution of textured α-uranium. Acta Mater. 60, 702–715.
Knezevic, M., McCabe, R.J., Tomé, C.N., Lebensohn, R.A., Chen, S.R., Cady, C.M., Gray Iii, G.T., Mihaila, B., 2013. Modeling mechanical response and texture evolution of α-uranium as a function of strain rate and temperature using polycrystal plasticity. Int. J. Plast. 43, 70–84.
Knezevic, M., Beyerlein, I.J., Lovato, M.L., Tomé, C.N., Richards, A.W., McCabe, R.J., 2014a. A strain-rate and temperature dependent constitutive model for BCC metals incorporating non-Schmid effects: application to tantalum–tungsten alloys. Int. J. Plast. 62, 93–104.
Knezevic, M., Drach, B., Ardeljan, M., Beyerlein, I.J., 2014b. Three dimensional predictions of grain scale plasticity and grain boundaries using crystal plasticity finite element models. Comput. Methods Appl. Mech. Eng. 277, 239–259.
Knezevic, M., Nizolek, T., Ardeljan, M., Beyerlein, I.J., Mara, N.A., Pollock, T.M., 2014c. Texture evolution in two-phase Zr/Nb lamellar composites during accumulative roll bonding. Int. J. Plast. 57, 16–28.
Knezevic, M., Zecevic, M., Beyerlein, I.J., Bhattacharyya, A., McCabe, R.J., 2015. Predicting texture evolution in Ta and Ta-10W alloys using polycrystal plasticity. JOM 67, 2670–2674.
Knezevic, M., Crapps, J., Beyerlein, I.J., Coughlin, D.R., Clarke, K.D., McCabe, R.J., 2016a. Anisotropic modeling of structural components using embedded crystal plasticity constructive laws within finite elements. Int. J. Mech. Sci. 105, 227–238.
Knezevic, M., Daymond, M.R., Beyerlein, I.J., 2016b. Modeling discrete twin lamellae in a microstructural framework. Scr. Mater. 121, 84–88.
Kúdela, S., Rudajevová, A., Kúdela, S., 2007. Anisotropy of thermal expansion in Mg- and Mg4Li-matrix composites reinforced by short alumina fibers. Mater. Sci. Eng. A 462, 239–242.
Lebensohn, R.A., Tomé, C.N., 1993. A self-consistent anisotropic approach for the simulation of plastic deformation and texture development of polycrystals: application to zirconium alloys. Acta Metall. Mater. 41, 2611–2624.
Lebensohn, R.A., Zecevic, M., Knezevic, M., McCabe, R.J., 2016. Average intragranular misorientation trends in polycrystalline materials predicted by a viscoplastic self-consistent approach. Acta Mater. 104, 228–236.
Lee, N., D.Lee, D.N., Nam Han, H., 2015. Recrystallization Textures of Metals and Alloys.
Lentz, M., Klaus, M., Beyerlein, I.J., Zecevic, M., Reimers, W., Knezevic, M., 2015. In situ X-ray diffraction and crystal plasticity modeling of the deformation behavior of extruded Mg–Li–(Al) alloys: an uncommon tension–compression asymmetry. Acta Mater. 86, 254–268.
Lentz, M., Risse, M., Schaefer, N., Reimers, W., Beyerlein, I.J., 2016. Strength and ductility with {1011} - {1012} double twinning in a magnesium alloy. Nat. Commun. 7, 11068.
Lesuer, D.R., Syn, C.K., Sherby, O.D., Wadsworth, J., Lewandowski, J.J., Hunt, W.H., 1996. Mechanical behaviour of laminated metal composites. Int. Mater. Rev. 41, 169–197.
Li, L., Nagai, K., Yin, F., 2008. Progress in cold roll bonding of metals. Sci. Technol. Adv. Mater. 9 023001–023001.
Mara, N.A., Beyerlein, I.J., 2015. Interface-dominant multilayers fabricated by severe plastic deformation: stability under extreme conditions. Curr. Opin. Solid State Mater. Sci. 19, 265–276.
Milner, D., VAIDYANATH, L., 1960. Significance of surface preparation in cold pressure welding. Met. Constr. Br. Weld. J. 7, 1–6.
Misra, A., Hoagland, R.G., 2007. Plastic flow stability of metallic nanolaminate composites. J. Mater. Sci. 42, 1765–1771.

Motevalli, P.D., Eghbali, B., 2015. Microstructure and mechanical properties of Tri-metal Al/Ti/Mg laminated composite processed by accumulative roll bonding. Mater. Sci. Eng. A 628, 135–142.
Nguyen-Minh, T., Sidor, J., Petrov, R., Kestens, L., 2015. Shear banding and its contribution to texture evolution in rotated Goss orientations of BCC structured materials. In: IOP Conference Series: Materials Science and Engineering. IOP Publishing, P. 012023.
Niessen, A.K., de Boer, F.R., Boom, R., de Châtel, P.F., Mattens, W.C.M., Miedema, A.R., 1983. Model predictions for the enthalpy of formation of transition metal alloys II. Calphad 7, 51–70.
Pathak, S., Velisavljevic, N., Baldwin, J.K., Jain, M., Zheng, S., Mara, N.A., Beyerlein, I.J., 2017. Strong, ductile, and thermally stable bcc-Mg nanolaminates. Sci. Rep. 7, 8264.
Pu, C., Gao, Y., 2015. Crystal plasticity analysis of stress partitioning mechanisms and their microstructural dependence in advanced steels. J. Appl. Mech. 82 031003–031003-031006.
Raabe, D., Lücke, K., 1994a. Rolling textures of niobium and molybdenum. Z. Met. 85, 302–306.
Raabe, D., Luecke, K., 1994b. Rolling and annealing textures of bcc metals. Mater. Sci. Forum. In: Proceedings of the 10th International Conference on Textures of Materials. Part 1 (Of 2), Sep 20-24 1993 157-6, 597–610.
Risse, M., Lentz, M., Fahrenson, C., Reimers, W., Knezevic, M., Beyerlein, I.J., 2017. Elevated temperature effects on the plastic anisotropy of an extruded Mg-4 Wt pct Li alloy: experiments and polycrystal modeling. Metall. Mater. Trans. A 48, 446–458.
Saito, Y., Utsunomiya, H., Tsuji, N., Sakai, T., 1999. Novel ultra-high straining process for bulk materials-development of the accumulative roll-bonding (ARB) process. Acta Mater. 47, 579–583.
Savage, D.J., Beyerlein, I.J., Knezevic, M., 2017. Coupled texture and non-Schmid effects on yield surfaces of body-centered cubic polycrystals predicted by a crystal plasticity finite element approach. Int. J. Solids Struct. 109, 22–32.
Savage, D.J., Chandola, N., Cazacu, O., McWilliams, B.A., Knezevic, M., 2018. Validation of recent analytical dilatational models for porous polycrystals using crystal plasticity finite element models with Schmid and non-Schmid activation laws. Mech. Mater. 126, 148–162.
Song, G., Li, T., Yu, J., Liu, L., 2018. A review of bonding immiscible Mg/steel dissimilar metals. Materials 11, 2515.
Sun, Y.F., Tsuji, N., Fujii, H., Li, F.S., 2010. Cu/Zr nanoscaled multi-stacks fabricated by accumulative roll bonding. Journal of Alloys and Compounds 504. Le Supplément 1, S443–S447.
Takajo, S., Vogel, S.C., Tomé, C.N., 2019. Viscoplastic self-consistent polycrystal modeling of texture evolution of ultra-low carbon steel during cold rolling. Model. Simul. Mater. Sci. Eng. 27, 045003.
Tayyebi, M., Eghbali, B., 2013. Study on the microstructure and mechanical properties of multilayer Cu/Ni composite processed by accumulative roll bonding. Mater. Sci. Eng. A 559, 759–764.
Tomé, C.N., 1999. Self-consistent polycrystal models: a directional compliance criterion to describe grain interactions. Model. Simul. Mater. Sci. Eng. 7, 723–738.
Tromans, D., 2011. Elastic Anisotropy of HCP Metal Crystals and Polycrystals.
Turner, P.A., Tomé, C.N., 1994. A study of residual stresses in Zircaloy-2 with rod texture. Acta Metall. Mater. 42, 4143–4153.
Valiev, R.Z., Islamgaliev, R.K., Alexandrov, I.V., 2000. Bulk nanostructured materials from severe plastic deformation. Prog. Mater. Sci. 45, 103–189.
Vogel, S.C., Hartig, C., Lutterotti, L., Von Dreele, R.B., Wenk, H.R., Williams, D.J., 2004. Texture measurements using the new neutron diffractometer HIPPO and their analysis using the Rietveld method. Powder Diffr. 19, 65–68.
Wang, Z.Q., Beyerlein, I.J., 2011. An atomistically-informed dislocation dynamics model for the plastic anisotropy and tension–compression asymmetry of BCC metals. Int. J. Plast. 27, 1471–1484.
Wang, Y.N., Huang, J.C., 2003. Texture analysis in hexagonal materials. Mater. Chem. Phys. 81, 11–26.
Wang, K., Reeber, R.R., 1998. The role of defects on thermophysical properties: thermal expansion of V, Nb, Ta, Mo and W. Mater. Sci. Eng. R Rep. 23, 101–137.
Wenk, H.R., Lutterotti, L., Vogel, S., 2003. Texture analysis with the new HIPPO TOF diffractometer. Nucl. Instrum. Methods Phys. Res. Sect. A Accel. Spectrom. Detect. Assoc. Equip. 515, 575–588.
Yahiro, A., Masui, T., Yoshida, T., 1991. Development of nonferrous clad plate and sheet by warm rolling with different temperature of materials. ISIJ Int. 31, 647–654.
Yang, D., Cizek, P., Hodgson, P., Wen, C.e., 2010. Ultrafine equiaxed-grain Ti/Al composite produced by accumulative roll bonding. Scr. Mater. 62, 321–324.
Yasuda, M., Kikuchi, S., 2004. Effect of annealing on the strength of Ag/Fe and Ag/Ni super-laminates produced by foil metallurgy. Mater. Sci. Eng. A 387–389, 783–788.
Yazar, Ö., Ediz, T., Öztürk, T., 2005. Control of macrostructure in deformation processing of metal/metal laminates. Acta Mater. 53, 375–381.
Zare, H., Jahedi, M., Toroghinejad, M.R., Meratian, M., Knezevic, M., 2016a. Compressive, shear, and fracture behavior of CNT reinforced Al matrix composites manufactured by severe plastic deformation. Mater. Des. 106, 112–119.
Zare, H., Jahedi, M., Toroghinejad, M.R., Meratian, M., Knezevic, M., 2016b. Microstructure and mechanical properties of carbon nanotubes reinforced aluminum matrix composites synthesized via equal-channel angular pressing. Mater. Sci. Eng. A 670, 205–216.
Zecevic, M., Knezevic, M., 2017. Modeling of sheet metal forming based on implicit embedding of the elasto-plastic self-consistent formulation in shell elements: application to cup drawing of AA6022-T4. JOM 69, 922–929.
Zecevic, M., Knezevic, M., 2019. An implicit formulation of the elasto-plastic self-consistent polycrystal plasticity model and its implementation in implicit finite elements. Mech. Mater. 136, 103065.
Zecevic, M., Knezevic, M., Beyerlein, I.J., Tomé, C.N., 2015. An elasto-plastic self-consistent model with hardening based on dislocation density, twinning and de-twinning: application to strain path changes in HCP metals. Mater. Sci. Eng. A 638, 262–274.
Zecevic, M., Beyerlein, I.J., Knezevic, M., 2017a. Coupling elasto-plastic self-consistent crystal plasticity and implicit finite elements: applications to compression, cyclic tension-compression, and bending to large strains. Int. J. Plast. 93, 187–211.
Zecevic, M., Pantleon, W., Lebensohn, R.A., McCabe, R.J., Knezevic, M., 2017b. Predicting intragranular misorientation distributions in polycrystalline metals using the viscoplastic self-consistent formulation. Acta Mater. 140, 398–410.
Zecevic, M., Beyerlein, I.J., Knezevic, M., 2018a. Activity of pyramidal I and II < c+a > slip in Mg alloys as revealed by texture development. J. Mech. Phys. Solids 111, 290–307.
Zecevic, M., Lebensohn, R.A., McCabe, R.J., Knezevic, M., 2018b. Modeling of intragranular misorientation and grain fragmentation in polycrystalline materials using the viscoplastic self-consistent formulation. Int. J. Plast. 109, 193–211.
Zecevic, M., Lebensohn, R.A., McCabe, R.J., Knezevic, M., 2019. Modelling recrystallization textures driven by intragranular fluctuations implemented in the viscoplastic self-consistent formulation. Acta Mater. 164, 530–546.
Zeng, L.F., Gao, R., Fang, Q.F., Wang, X.P., Xie, Z.M., Miao, S., Hao, T., Zhang, T., 2016. High strength and thermal stability of bulk Cu/Ta nanolamellar multilayers fabricated by cross accumulative roll bonding. Acta Mater. 110, 341–351.